SINTEF

SINTEF F19941- Confidential

Report

Analysis of Terrain Induced Turbulence on Alternative Airport Locations at the Faroe Islands using Numerical Simulations

Author(s)
Adil Rasheed, SINTEF ICT
Karstein Sørli, SINTEF ICT
Knut Helge Midtbø, The Norwegian Meteorological Institute

SINTEF ICT
Applied Mathematics
2011-07-06

SINTEF IKT
SINTEF ICT

Address:
Postboks 4760 Sluppen
NO-7465 Trondheim
NORWAY

Telephone:+47 73593000
Telefax:+47 73592971

postmottak.IKT@sintef.no
www.sintef.no
Enterprise /VAT No:
NO 948 007 029 MVA

KEYWORDS:
Airport citing
Terrain-forced turbulence
Flow simulations

Report

Analysis of Terrain Induced Turbulence on Alternative Airport Locations at the Faroe Islands using Numerical Simulations

VERSION

DATE
2011-07-06

AUTHOR(S)
Adil Rasheed
Karstein Sørli
Knut Helge Midtbø

CLIENT(S)
Faroe Islands, Harbour Department

CLIENT'S REF.
Klæmint Østerø

PROJECT NO.
90A348.06

NUMBER OF PAGES/APPENDICES:
35 / 0

ABSTRACT
In this study we have presented and analyzed the computer simulations conducted to investigate the terrain induced turbulence at three alternate locations at The Faroe Islands: Glyvursnes, Søltuvik and Vágar, as a potential site for a new airport. We give a brief description of the governing equations of atmospheric flow which are key elements to evaluating the flight conditions at a particular site. We also describe the safety criteria that we use to quantify the potential risk for the aviation activities. A description of domain size and mesh is given along with the profiles of velocity components and turbulent kinetic energy used to describe the boundary conditions for the governing equations. The numerical simulations are discussed and explained. Finally the conclusions from the study are presented.

The *Glyvursnes* location is the best of the three alternatives with respect to the given criteria. The reasons according to the study are the aerodynamic shape of the coastal region to the south, north and east of the runway and its location far away from the cliffs on the western side. *Søltuvik* has unfavorable flight conditions due to the cliff on the western side which has a strong local effect and the high hill on the north-eastern side which causes much larger scale phenomenon. The third location *Vágar* is also surrounded by hills on the north and south side. From the simulation it appears that the northerly, north-easterly, southerly and south-westerly are problematic wind directions.

PREPARED BY
Adil Rasheed

SIGNATURE

CHECKED BY
Svein Nordenson

SIGNATURE

APPROVED BY
Roger Bjørgan

SIGNATURE

REPORT NO.
SINTEF F19941

ISBN

CLASSIFICATION
Confidential

CLASSIFICATION THIS PAGE
Confidential

Contents

1 Introduction

The Faroe Islands are an island group situated between the Norwegian Sea and the North Atlantic Ocean, approximately halfway between Great Britain and Iceland. The islands are characterized by a very uneven terrain and the shorelines by sharp cliffs. Since the island group is isolated from any mainland, air and sea travel are the only mode of transportation of goods and people to and from the islands. At the moment the only airport serving the island is located at Vágar. Efforts are on to identify other potential locations for new airports. The uneven terrain induces air turbulence which is a potential hazard for the aviation activities.

Figure 1: Location of Glyvursnes, Søltuvik and Vágar at The Faroe Islands. The image of the group of island is found at http://www.lonelyplanet.com/maps/europe/faroe-islands/ and the actual locations are included.

In this study we have presented and analyzed the computer simulations conducted to investigate the terrain induced turbulence at three alternate locations: Glyvursnes, Søltuvik and Vágar, as a potential site for the new airport on the Faroe Islands (see figure 1). In Section 2 we give a brief description of the governing equations of atmospheric flow which are key to evaluating the flight conditions at a particular site. Numerics of the computation is also described. Finally in the same section we describe the safety criteria that we use to quantify the potential risk for the aviation activities. In Section 3 a description of the domain size and mesh is given along with the profiles of velocity components and turbulent kinetic energy used to describe the boundary conditions for the governing equations. This is followed by the Section 4 where the results from the numerical simulations are discussed and explained. Finally the conclusions from the study have been presented in Section 5.

2 Theory

2.1 Governing Equations

The equation of motion for incompressible flow may be generalized to atmospheric flows by the use of the so-called anelastic approximation. This formulation is often applied in meteorological models, and may be written in the following conservative form ([1] and [3]).

$$\nabla \cdot (\rho_s \mathbf{u}) = 0 \tag{1}$$

$$\frac{D\mathbf{u}}{Dt} = -\nabla \left(\frac{p_d}{\rho_s} \right) + \mathbf{g}\frac{\theta_d}{\theta_s} + \frac{1}{\rho_s}\nabla \cdot \tau + \mathbf{f} \tag{2}$$

$$\frac{D\theta}{Dt} = \nabla \cdot (\gamma \nabla \theta) + q \tag{3}$$

Here $(\mathbf{u}, p, \theta, \rho)$ represent velocity, pressure, potential temperature and density, respectively. Furthermore, τ is the stress tensor, $\mathbf{f}$ is a source term that may include rotational effects, $\mathbf{g}$ is the gravitational acceleration, γ is the thermal diffusivity and q is the energy source term. Subscript s indicates hydrostatic values and subscript d the deviation between the actual value and its hydrostatic part, i.e. $p = p_s + p_d$, $\theta = \theta_s + \theta_d$, $\rho = \rho_s + \rho_d$, where the hydrostatic part is given by $\partial p_s / \partial z = -g\rho_s$. In addition, the following expression for hydrostatic density may be derived from the state equation and the definition of potential temperature:

$$\rho_s = \frac{p_s}{R\theta_s} \left(\frac{p_o}{p_s} \right)^{R/C_p} \tag{4}$$

where R is the gas constant and C_p is the specific heat at constant pressure. Hence, once the hydrostatic (potential) temperature profile is given, the hydrostatic pressure and density may be calculated, and then substituted into Equations 1 and 2.

It may be noted that the Boussinesq approximation is obtained from the system of Equations 1 and 2 by assuming constant values (ρ_o, θ_o) instead of the hydrostatic values, and that formulation may well be used for incompressible flow at ordinary temperature.

The aim of the present study is to solve these equations for high Reynolds-number flows. For this purpose we apply an unsteady Reynolds-averaged modeling of the equation system, together with a turbulence model. Presently a standard high-Reynolds $(k - \epsilon)$ turbulence model is used for this purpose. With these assumptions the model equations take the following form:

$$\nabla \cdot (\rho_s \mathbf{u}) = 0 \tag{5}$$

$$\frac{D\mathbf{u}}{Dt} = -\nabla \left(\frac{p_d}{\rho_s} \right) + \mathbf{g}\frac{\theta_d}{\theta_s} + \frac{1}{\rho_s}\nabla \cdot \mathbf{R} + \mathbf{f} \tag{6}$$

$$\frac{D\theta}{Dt} = \nabla \cdot (\gamma_T \nabla \theta) + q \tag{7}$$

$$\frac{DK}{Dt} = \nabla \cdot (\nu_T \nabla K) + P_k + G_\theta - \epsilon \tag{8}$$

$$\frac{D\epsilon}{Dt} = \nabla \cdot \left(\frac{\nu_T}{\sigma_e} \nabla \epsilon \right) + (C_1 P_k + C_3 G_\theta)\frac{\epsilon}{k} - C_2 \frac{\epsilon^2}{k} \tag{9}$$

where turbulent viscosity is given by $\nu_T = C_\nu \frac{k^2}{\epsilon}$. The Reynolds stress tensor is given by

$$R_{ij} = \nu_T \left(\frac{\partial u_i}{\partial x_j} + \frac{\partial u_j}{\partial x_i} \right) - \frac{2}{3} k \delta_{ij} \tag{10}$$

while the eddy diffusivity appearing in the energy equation is $\gamma_T = \nu_T/\sigma_T$, σ_T being the turbulent Prandtl number. The production and stratification terms in the turbulence model are given by

$$P_k = \nu_T \left(\frac{\partial u_i}{\partial x_j} + \frac{\partial u_j}{\partial x_i} \right) \frac{\partial u_i}{\partial x_j}, \quad G_\theta = -\frac{g}{\theta} \frac{\nu_T}{\sigma_T} \frac{\partial \theta}{\partial z} \tag{11}$$

Conventional constants for the high-Reynolds $(k-\epsilon)$ model are given by

$$(C_\nu, C_1, C_2, \sigma_e) = (0.09, 1.44, 1.92, 1.3) \tag{12}$$

The value for C_3 is more uncertain. In the present study we assume $C_3 G_\theta = \max(G_\theta, 0)$, i.e. $C_3 = 0$ in stably stratified flows, else $C_3 = 1$ ([7]).

2.2 Algebraic formulation

The governing equations presented in the last section are discretized in space by the use of a finite element method, and the time integration is performed using a semi-implicit two-level formulation. In the compressed form the discretized equation system can be written in the following form:

$$\left[\frac{1}{\Delta t} \mathbf{M} + \alpha \mathbf{A}_u^* \right] \Delta \mathbf{u}^{n+1} = -\mathbf{A}_u^* \mathbf{u}^n + \mathbf{s}_u^n - \mathbf{C} \left(\frac{p}{\rho_s} \right)^{n+1} \tag{13}$$

$$\mathbf{C}^T \rho_s \mathbf{u}^{n+1} = 0 \tag{14}$$

$$\left[\frac{1}{\Delta t} \mathbf{M} + \alpha \mathbf{A}_\phi^* \right] \Delta \phi^{n+1} = -\mathbf{A}_\phi^* + \mathbf{s}_\phi^n \tag{15}$$

Here $\mathbf{M}$ represents the mass matrix, $\mathbf{A}$ is the sum of diffusion and advection matrices (subscripts indicating the actual variable), $\mathbf{C}$ in the gradient matrix, and $\mathbf{s}$ (with subscripts) represents source terms. The implicit parameter α may be chosen in the interval $(1/2, 1)$, and $\mathbf{A}^*$ indicates the advection velocity taken at $\mathbf{u}^{n+\alpha}$. The variables $(\mathbf{u}, \mathbf{p})$ are redefined here as nodal vectors for velocity and pressure, and ϕ represents nodal vectors for each of the scalar variables (θ, K, ϵ). The increments are defined by $\delta \mathbf{u}^{n+1} = \mathbf{u}^{n+1} - \mathbf{u}^n$, $\delta \phi^{n+1} = \phi^{n+1} - \phi^n$, where superscripts indicate time levels.

2.3 Segregated implicit projection algorithm

In this study we use a segregated, implicit projection method that is non-iterative, with corrections within each time-step. This algorithm has several features in common with the SIMPLER-like pressure projection method described in [5], but instead of iterations it applies corrections similar to the PISO method. The algorithm is given by the following steps:

1. Predict the pressure field via a pseudo-velocity prediction from the system

$$\tilde{\mathbf{M}} = \Delta \hat{\mathbf{u}} = -\mathbf{A}_u \mathbf{u}^n + s_u; \quad \Delta \hat{\mathbf{u}} = \hat{\mathbf{u}} - \mathbf{u}^n, \tag{16}$$

$$L p^* = \mathbf{C}^T \rho_s \hat{\mathbf{u}} \tag{17}$$

   where L represents a discretized Laplacian operator.

2. Compute the velocity field from the (semi)implicit momentum equation

$$\left[\tilde{\mathbf{M}} + \alpha \mathbf{A}_u^* \right] \Delta \mathbf{u}^* = -\mathbf{A}_u u^n + s_u - \mathbf{C} \left(\frac{p}{\rho_s} \right)^*; \quad \Delta \mathbf{u}^* = \mathbf{u}^* - \mathbf{u}^n \tag{18}$$

3. Compute (semi) implicit equations for other scalar quantities (k, ϵ, θ)

$$\left[\tilde{\mathbf{M}} + \alpha \mathbf{A}_\phi^* \right] \Delta \phi^{n+1} = -\mathbf{A}_\phi \phi^n + s_\phi; \quad \Delta \phi^{n+1} = \phi^{n+1} - \phi^n \tag{19}$$

Table 1: Domain size and mesh

-	Glyvursnes	Søltuvik	Vágar
Domain size (km)	$26 \times 14 \times 1.5$	$17.5 \times 15 \times 1.5$	$11 \times 8 \times 1.5$
$nx \times ny \times nz$	$290 \times 170 \times 41$	$180 \times 200 \times 41$	$120 \times 130 \times 41$

4. Correct the velocity and pressure fields by use of the projection step

$$L\Delta p^{n+1} = \mathbf{C}^T \rho_s \mathbf{u}^*; \quad p^{n+1} = p^* + \Delta p^{n+1} \tag{20}$$

$$\tilde{\mathbf{M}}(\rho_s \mathbf{u}^{n+1} - \rho_s \mathbf{u}^*) = -C\Delta p^{n+1} \tag{21}$$

The advection matrix A^* indicate use of a time-centeres advection velocity, which may be calculated as $u^{n+\alpha} = (1-\alpha)u^n + \alpha u^{n-1}$. Further, $\tilde{M} = M/\Delta t$ and the mass matrix may be lumped.

More details, description and validation results can be found in [8] and [9].

2.4 Safety Analysis

The simplest meteorological variable considered most important for aviation safety is called the $F-$factor or wind shear and what is called turbulence, represented by $\epsilon^{1/3}$. These quantities are given by Equations 22 and 23

$$F = -\overline{\frac{c}{g}\frac{\partial u}{\partial x} + \frac{w}{c}}^{\ell_f} = -\frac{c}{g\ell_f}[u(x+\ell_f/2 - u(x-\ell_f/2)t] + \frac{\overline{w}^{\ell_f}}{c} \tag{22}$$

$$\epsilon^{1/3} \approx \left(\frac{(C_\mu^{1/2}K)^{3/2}}{\ell_t}\right)^{1/3} \approx 0.67 K^{1/2}\ell_t^{-1/3} \tag{23}$$

Here c is the fly path, g is the acceleration due to gravity, u is the wind component along the fly path, w is the vertical wind component, ϵ is the turbulent dissipation, K is turbulent kinetic energy, ℓ_t turbulent length scale and ℓ_f is the minimum response distance for landing configuration and is of the order of $\sim 500\,m$, which corresponds to a time interval of about $t = O(7\,s)$. Averaging over this distance is indicated by the overline. Coefficient C_μ is given by $C_\mu \approx 0.09$. A good review of this theory can be found in the paper by [4].

Prevalence of the two conditions $F < -0.1$ and $\epsilon^{1/3} > 0.5\,m^{2/3}s^{-1}$ correspond to severe turbulence for commercial aircrafts and represent potential danger ([2]). These conditions are easily met when $\sqrt{K} > 3\,ms^{-1}$.

3 Simulation setup

A good choice of domain size, mesh resolution and boundary conditions was the prerequisites to a successful study. For the study we used the terrain data provided at a resolution of $5m \times 5m$. More elaborate information about the domain, mesh and boundary conditions are provided in the following subsections.

3.1 Domain size and mesh

Table 1 gives the extent of the domain simulated, number of mesh points in the three directions for the three locations. The mesh was intentionally refined in the regions (see Figures 2, 3 and 4) where the variation in the topography was steep to resolve the local phenomenon taking place in the vicinity. In the vertical direction 41 levels with a stretching factor of 1.1 were used to discretize a vertical expanse of $1500\,m$. This resulted in a vertical resolution of about $1.5\,m$ near the ground and $300\,m$ near the top of the domain.

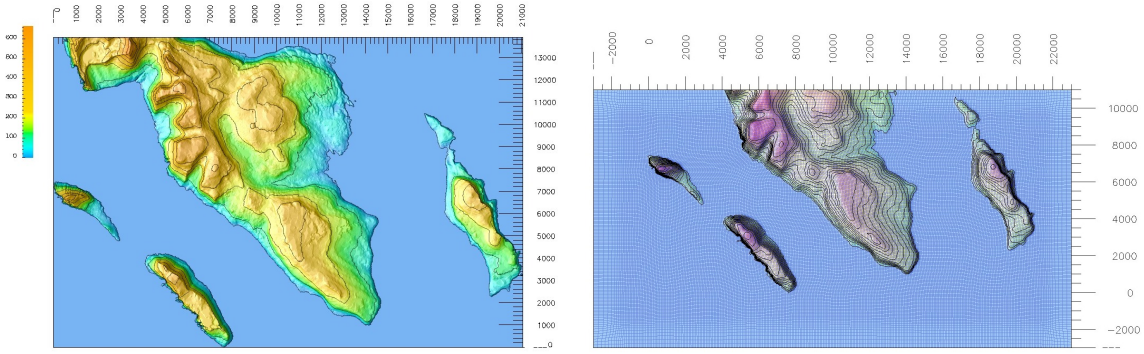

(a) Terrain (b) Mesh

Figure 2: Terrain and mesh for Glyvursnes

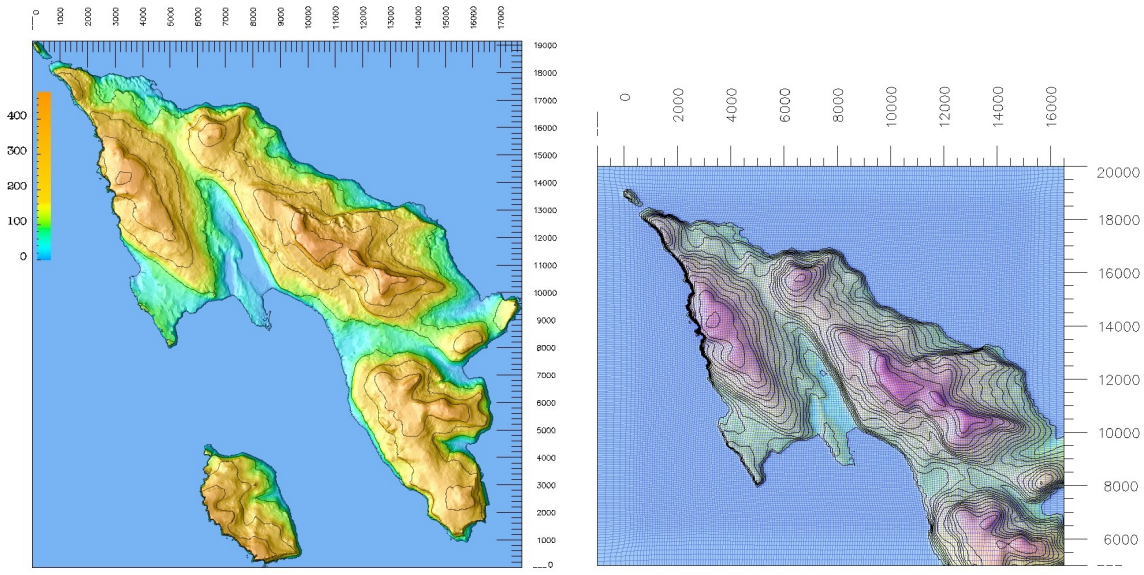

(a) Terrain (b) Mesh

Figure 3: Terrain and mesh for Søltuvik

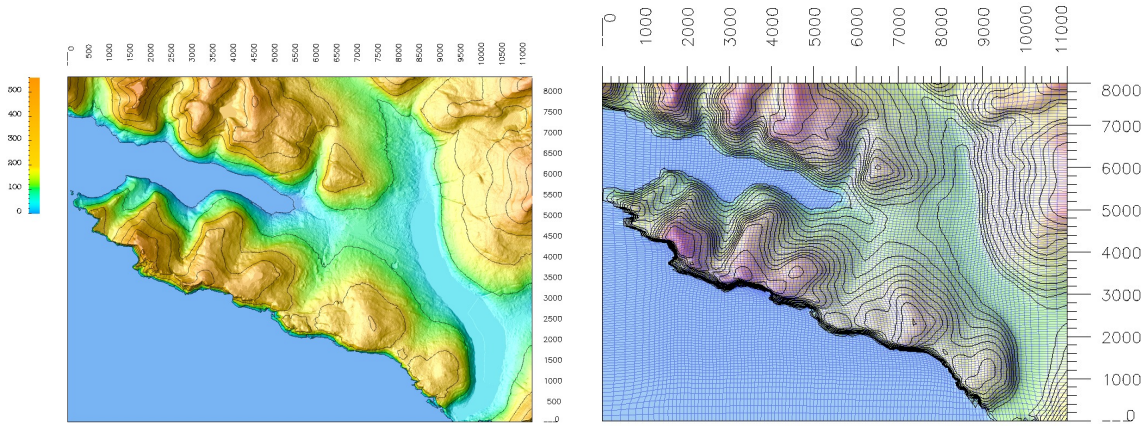

(a) Terrain (b) Mesh

Figure 4: Terrain and mesh for Váger

3.2 Boundary conditions

In complicated mountainous terrain it is generally difficult to specify a realistic inlet profile for the quantities we want to solve for without the availability of meteorological quantities from a larger scale model. In the absence of a realistic boundary condition in this study we have made a slight compromise and used a standard profile for wind speed and turbulent kinetic energy to specify the boundary conditions and initialize the domain. Considering the heterogeneity and uneveness in the terrain this should not undermine the importance of the study. The profiles for the wind speed $u_0(z)$ and turbulent kinetic energy $K_0(z)$ are given by

$$u_0(z) = \frac{u_*}{\kappa}\left(ln\frac{z}{z_0} + W\left(\frac{z}{D}\right)\right) \tag{24}$$

$$K(z) = C_\mu^{-1/2}u_*^2\left(1 - \frac{z}{D}\right) \tag{25}$$

where u_*, z_0, z and D represent friction velocity, surface roughness, height above the ground surface and boundary layer thickness, respectively. The so-called wake function W is defined by the formula $W(z/D) = (A-1)(z/D) - A/2(z/D)^2$ such that $W(1) = 1$. The coefficients $\kappa = 0.42$ and $A = 4.0$. Synoptic wind (mesoscale) U is given by $U = u_0(D)$. In the present simulations we have used $(z_0, D, U) = (0.3\,m, 1500\,m, 20\,m/s)$ such that the friction velocity $u_* \approx 0.9\,m/s$ and wind speed $10\,m$ above the ground is $u_0 \approx 7.5\,m/s$. A surface roughness value of 0.001 have been used for the sea surface. Along with the magnitude, direction of the synoptic wind is also specified. Several simulations were conducted for different wind directions. The convention used in this report to specify the wind direction α is demonstrated in Figure 5 (a). It should be noted here that the meteorology and aviation community use a slightly different convention as shown in Figure 5(b). The simulations were conducted for eight different wind directions (W,SW,S,SE,E,NE,N,NW) for all the three alternate locations. All the simulations conducted and presented in this report are for neutral stratification and hence the results are scalable. Also considering the size of the length and velocity scales involved we can safely neglect the influence of the Coriolis force.

4 Results and Discussions

Generally a smooth variation in terrain (see Figure 6 top) leads to a laminar flow which is marked by low turbulence. However, things change dramatically when the terrain changes sharply (see Figure 6 bottom). When encountering a steep terrain the flow starts to accelerate in the vertical direction gaining significant vertical velocity component. Such flows are characterized by flow separation and formation of eddies near the edge as shown in the figure with an ellipse. Formation of such eddies is the primary reason for an increase

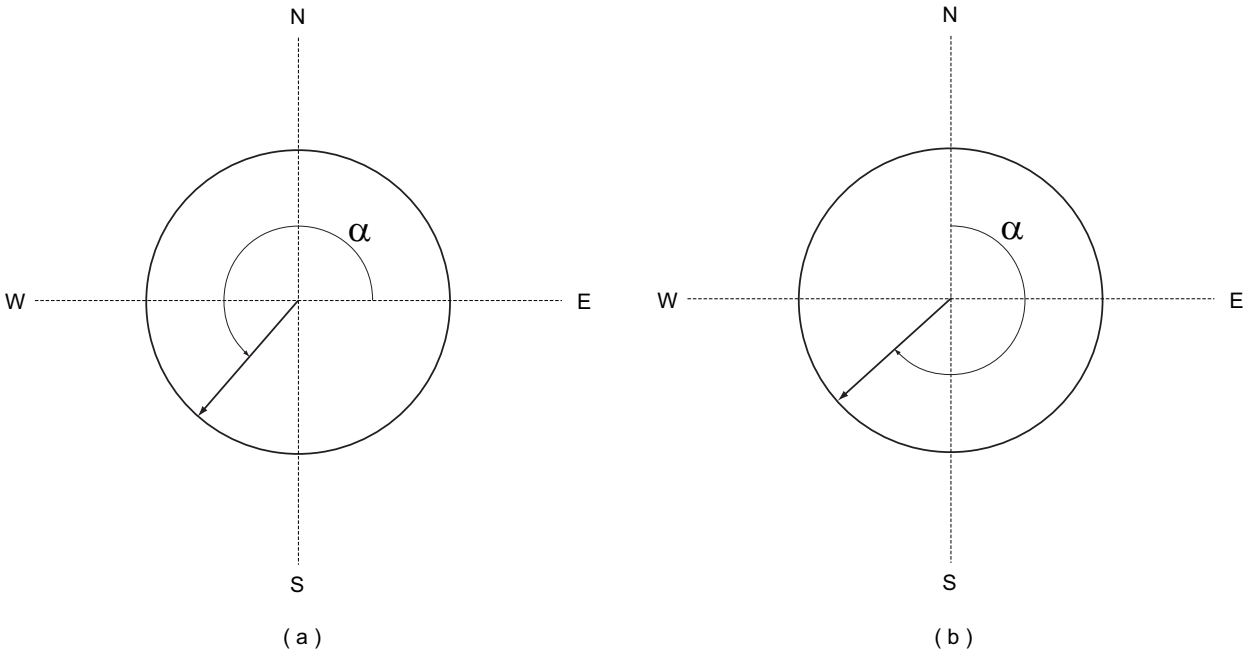

Figure 5: Conventions for wind direction. In (a) is shown the convention we use in our simulations, while (b) is the convention used by meteorology and aviation community.

in turbulence. These observations are well established through wind tunnel and numerical experiments. A similar trend is observed in the present study too. In this section we present the 3-D contours of the turbulent velocity $u_t = 2\,m/s$ and $u_t = 2.5\,m/s$. It should be reiterated that a value of $u_t = 3.5\,m/s$ and above can be potentially dangerous. Since the results are scalable, $u_t = 2.0\,m/s$ will become $u_t = 3.0\,m/s$ if the free airstream speed increases from $20\,m/s$ to $30\,m/s$. Below we present the important observations for each of the locations under the investigation. The vertical axis have been scaled by a factor of 4 for better visualization (the simulation was conducted with the actual vertical dimension).

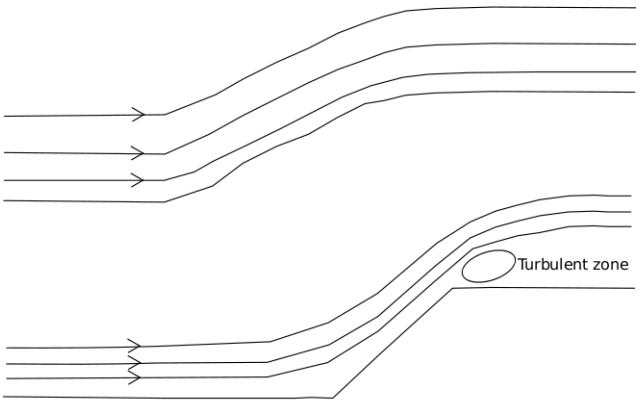

Figure 6: Flow separation and vortex formation

4.1 Glyvursnes

The characteristic wind data for Glyvursnes from a 2-year measurement campaign at the proposed airport location as reported in [6] shows that the dominant direction is within the sector SSW-W. However, this data was collected at $10m$ above the ground and could not be taken as a representative of the free stream wind (experience tells us that the wind speed at $10\,m$ above the ground can be influenced heavily by rotors and other local phenomena). Therefore, in order to make a thorough investigation we conducted eight simulations for different wind directions (W,SW,S,SE,E,NE,N and NW) covering the whole windrose.

4.1.1 Summary of the Glyvursnes simulations

A summary of the most important findings of the Glyvursnes simulations are enumerated below:

- For the westerly wind (Figure 7) the contour of $U_t = 2.0$ occurs on the southern side of the planned runway at an elevation of $20 - 100m$.
- For the southwesterly wind (Figure 8) the contour of $U_t = 2.0$ occurs at about $50 - 150\,m$ above the runway.
- For the southerly wind (Figure 9) the contour of $U_t = 2.0$ occurs at the cliff side south of the planned runway. This area is reasonably far away from the runway.
- For the southeasterly wind (Figure 10) very little turbulence is encountered close to the proposed runway. This is due to the fact that the air approaching the island encounters an aerodynamically favorable terrain. The air ascend along the terrain smoothly and there is no flow separation in the vicinity.
- For the easterly wind (Figure 11) the contour of $U_t = 2.0$ are approaching the north end of planned runway due to the presence of a smaller island on the east of the proposed runway.
- For the northeasterly wind (Figure 12) the contour of $U_t = 2.0$ are found south of the planned runway quite close to the ground.
- For the northerly wind (Figure 13) the contour of $U_t = 2.0$ lies on the north end and on the cliff on the south side of the planned runway.

4.2 Søltuvik

The characteristic wind data for Søltuvik from a 2-year measurement campaign at the proposed airport location as reported in [6] shows that the dominant direction within the sector S-W. However, as in the case of Glyvursnes this data was collected at $10m$ above the ground and could not be taken as a representative of the free stream wind. Therefore, as in the case of Glyvursnes we conducted eight simulations for different wind directions (W,SW,S,SE,E,NE,N and NW) covering the whole windrose.

4.2.1 Summary of the Søltuvik simulations

A summary of the most important findings of the Søltuvik simulations are enumerated below:

- For westerly wind (Figure 15) $U_t = 2.0$ contours are found near the east end of the planned runway.
- For southwesterly wind (Figure 16) the contours of $U_t = 2.5$ are starting to form on the steep cliff south of the planned runway. Two circular regions of $U_t = 2.2$ are found above the planned runway. Remark: The U_t values are expected to be even higher for a better resolution of the steep cliff of the peninsula on the southern side. At an elevation of $100 - 150\,m$ $U_t = 2.0 - 2.4$ contours are partly covering the planned runway.
- For southerly wind (Figure 17) two cliff-generated $U_t = 2.0$ regions are found close to the planned runway. A $U_t = 2.2$ region is found on the north end of the planned runway. At an elevation of $100\,m$ areas of U_t values in the range $2.0 - 2.5$ are found close to the northwestern end of the planned runway.

- For southeasterly wind (Figure 18) the cliff on the south-east side of the peninsula generates a $U_t = 2.0$ region on the southwest side of the planned runway.
- For easterly wind (Figure 19) $U_t = 2.0$ regions are found at the peninsula cliff and on parts close to the planned runway. A small $U_t = 2.5$ region forms at the cliff. Note the $U_t = 2.7$ regions east-southeast of the planned runway. Some computational uncertainties due to mountainous boundary could not be avoided.
- For northeasterly wind (Figure 20) the $U_t = 2.0$ region completely covers the planned runway, and the $U_t = 2.5$ regions are found on the west-northwestern side. Note $U_t = 3.0$ regions on the west-northwestern end of the planned runway. Regions at an elevation of $200\,m$ *gliding paths* on both side of the planned runway are covered by contours of U_t values in the range $2.0 - 2.8$.
- For northerly wind (Figure 21) the $U_t = 2.0$ region is formed above the planned runway. U_t regions in the range $2.0 - 2.4$ close to the west end of the planned runway, and $2.0 - 2.2$ above the runway. At an elevation of $300\,m$ and $350\,m$ U_t values in the range $2.0 - 2.5$ are found to the west of the planned runway. At elevation $250\,m$ U_t values in the range $2.0 - 2.5$ cover the western part of the planned runway. At elevations of $150\,m$ and $200\,m$ U_t values in the range $2.0 - 2.5$ nearly cover the planned runway. At an elevation of $100\,m$ small areas of $U_t \approx 2.0$ are found close to both ends of the planned runway.
- For northwesterly wind (Figure 22) along the planned runway there are U_t values in the range $1.7 - 2.2$. At elevation $100\,m$ streaks of $U_t \approx 2.4$ along the peninsula cliff are starting to form.

4.3 Vágar

4.3.1 Summary of the Vágar simulations

A summary of the most important findings of the Vágar simulations are enumerated below:

- For the westerly wind (Figure 23) the air flow encounters the sharp cliff and starts to ascend. This results in an intense turbulent zone on the leeward side of the hills close to the airport.
- The situation gets even worse when the wind is southwesterly (Figure 24) as in this case the wind approaches the sharp cliff orthogonally. Again the turbulent zone are confined close to the airport and also along the flying path.
- For the southerly wind (Figure 25) the situation is similar as the wind has to ascend the cliff resulting in rotors on the leeward side.
- For the southeasterly and easterly winds (Figures 26 and 27) , the flying conditions improve considerably. This is because the air flow takes place along the valleys and the turbulence if any is confined to the leeward side of the hills which in this case is reasonably far away from the airport and the flying path.
- For the north easterly wind (Figure 28) the turbulent zones are located on the north west side of the airport. This is the region through which aircrafts have to take off or land.
- For the northerly wind we did not conduct the simulation because we needed more terrain data to the north of the present domain in order to be able to apply a realistic boundary condition and resolve the hills to the north of the airport. However, from the large number of simulations we conducted during the study we can confidently deduce that turbulent zone will occur in the valley to the north west of the airport.
- For the northwesterly wind a scenario similar to that of south easterly wind (Figure 29) arises where the flow channels out through the valley posing no serious problem for aviation activities.

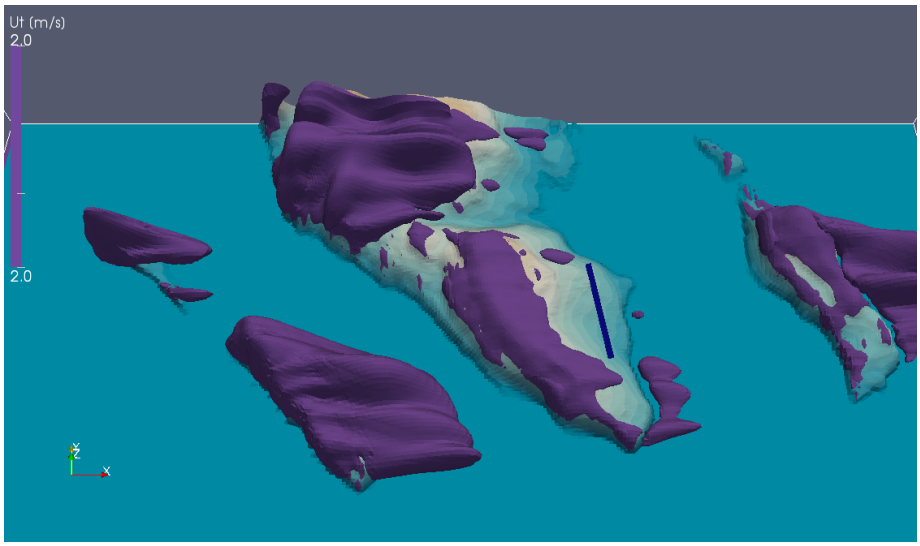

(a)

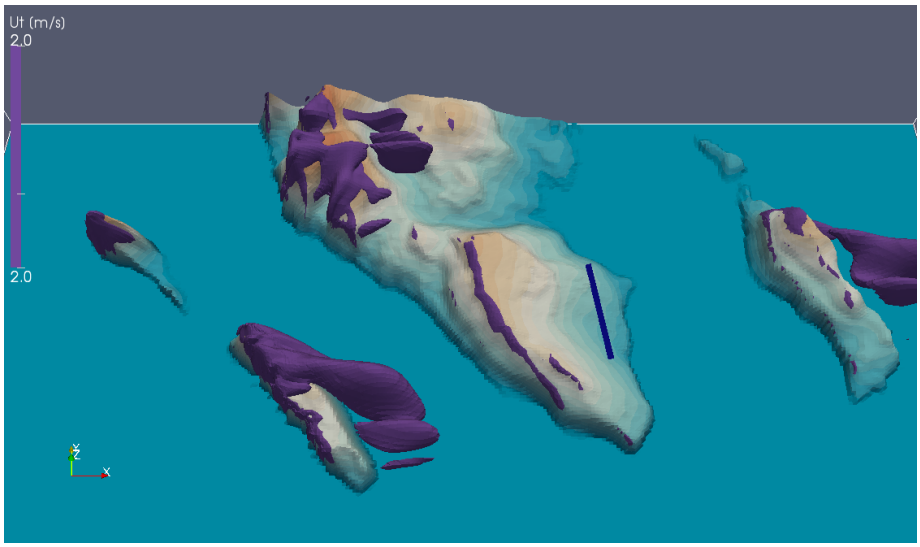

(b)

Figure 7: Iso-surfaces of turbulent velocity U_t at Glyvursnes for westerly wind ($\alpha = 0^o$). In (a) and (b) are shown iso-surfaces for $U_t = 2.0$ and $U_t = 2.5$, respectively.

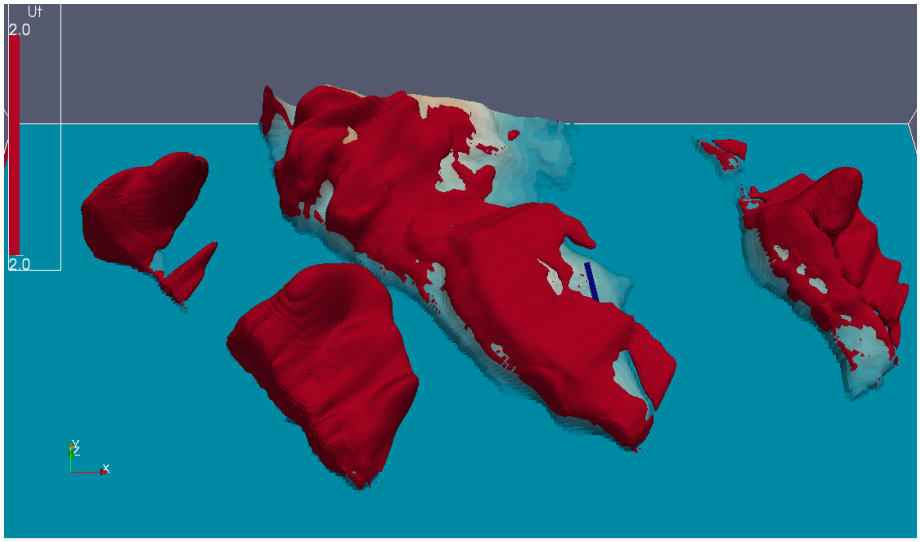

(a)

(b)

Figure 8: Iso-surfaces of turbulent velocity U_t at Glyvursnes for southwesterly wind ($\alpha = 45^o$). In (a) and (b) are shown iso-surfaces for $U_t = 2.0$ and $U_t = 2.5$, respectively.

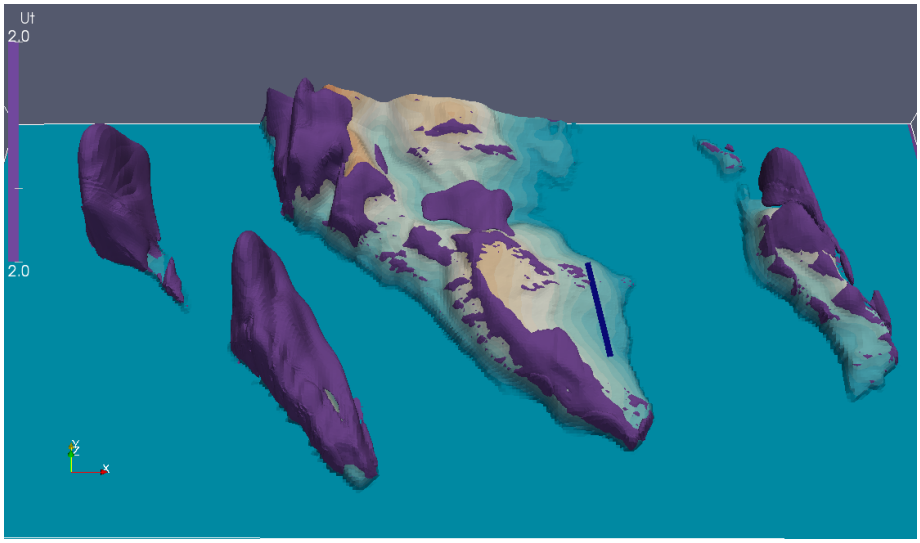

(a)

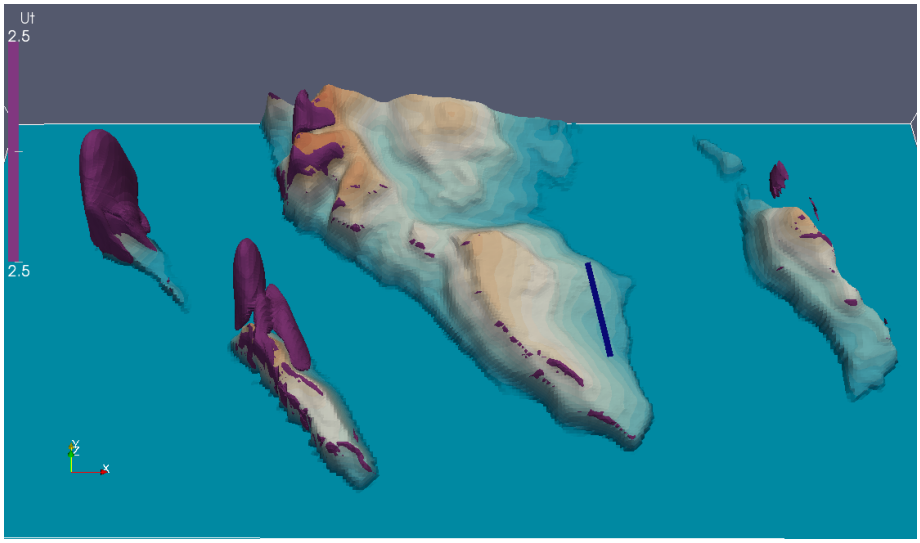

(b)

Figure 9: Iso-surfaces of turbulent velocity U_t at Glyvursnes for southerly wind ($\alpha = 90^o$). In (a) and (b) are shown iso-surfaces for $U_t = 2.0$ and $U_t = 2.5$, respectively.

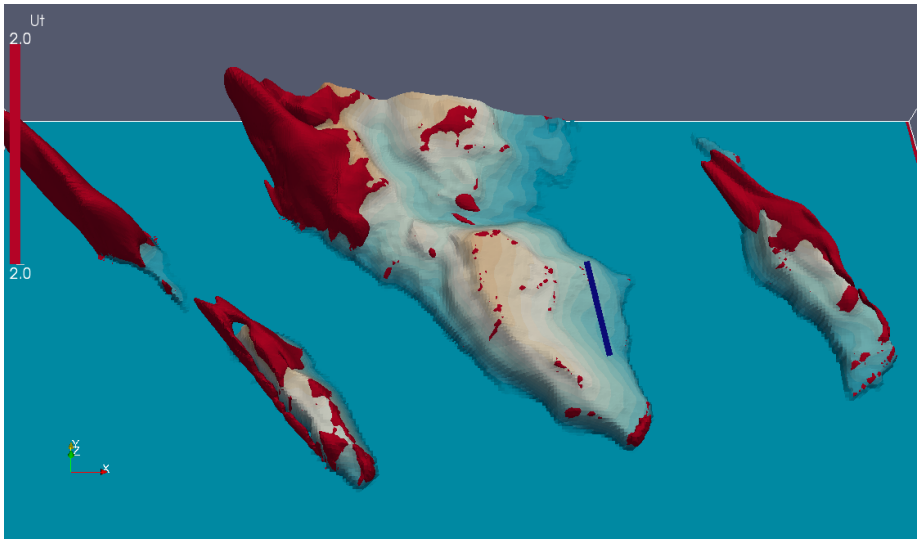

(a)

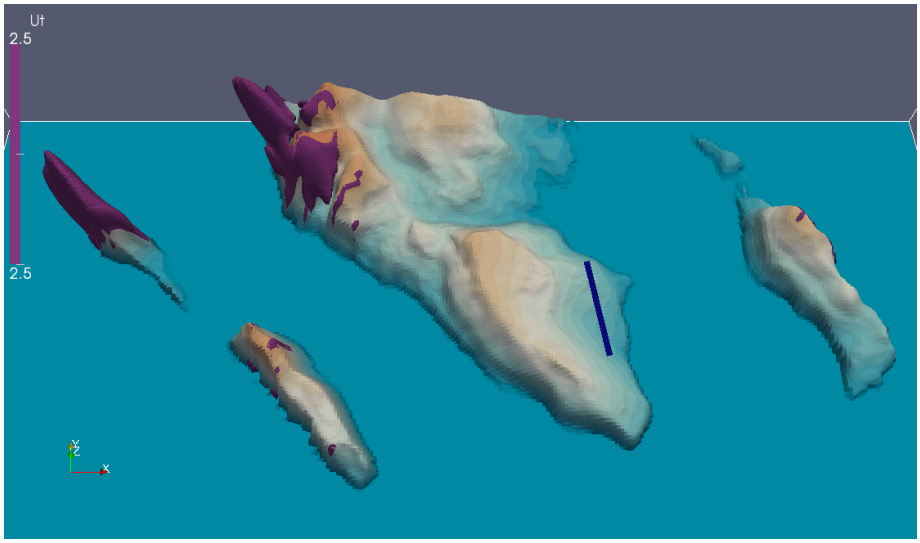

(b)

Figure 10: Iso-surfaces of turbulent velocity U_t at Glyvursnes for southeasterly wind ($\alpha = 135^o$). In (a) and (b) are shown iso-surfaces for $U_t = 2.0$ and $U_t = 2.5$, respectively.

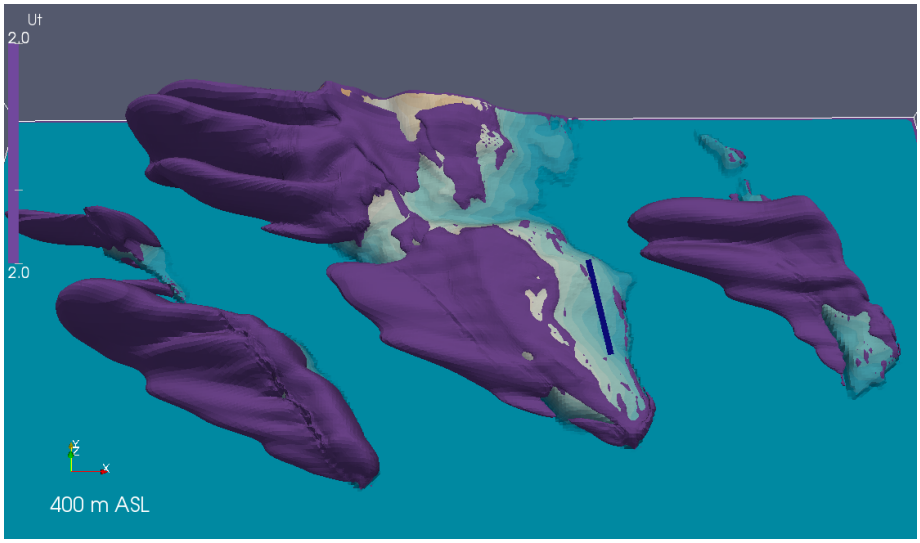

(a)

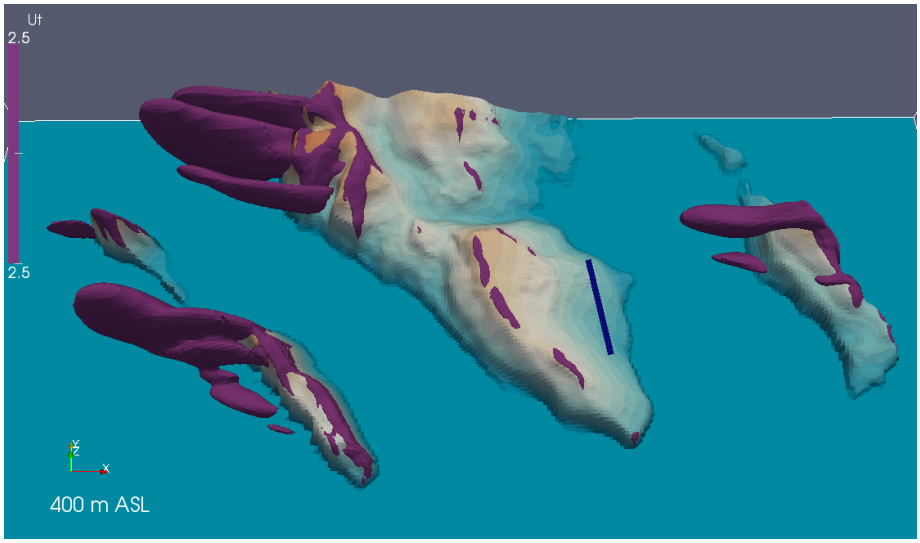

(b)

Figure 11: Iso-surfaces of turbulent velocity U_t at Glyvursnes for easterly wind ($\alpha = 180^o$). In (a) and (b) are shown iso-surfaces for $U_t = 2.0$ and $U_t = 2.5$, respectively.

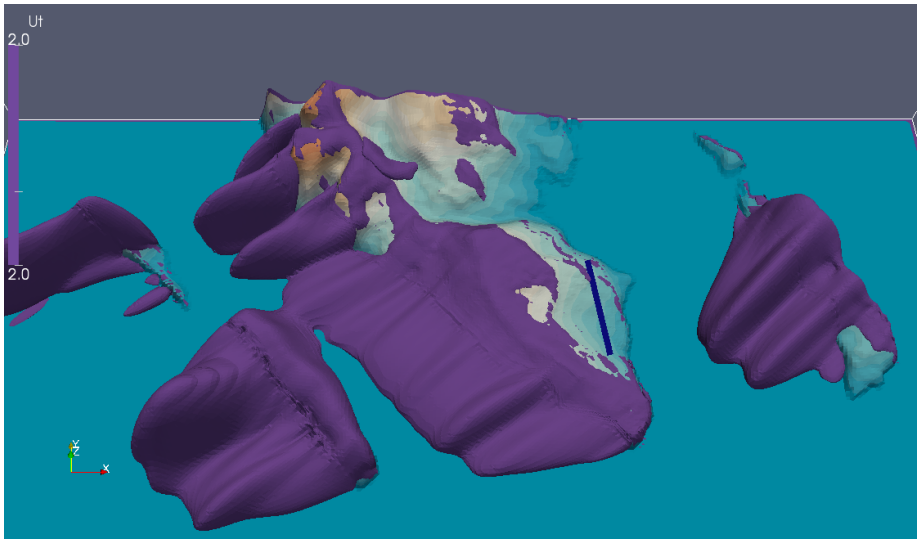

(a)

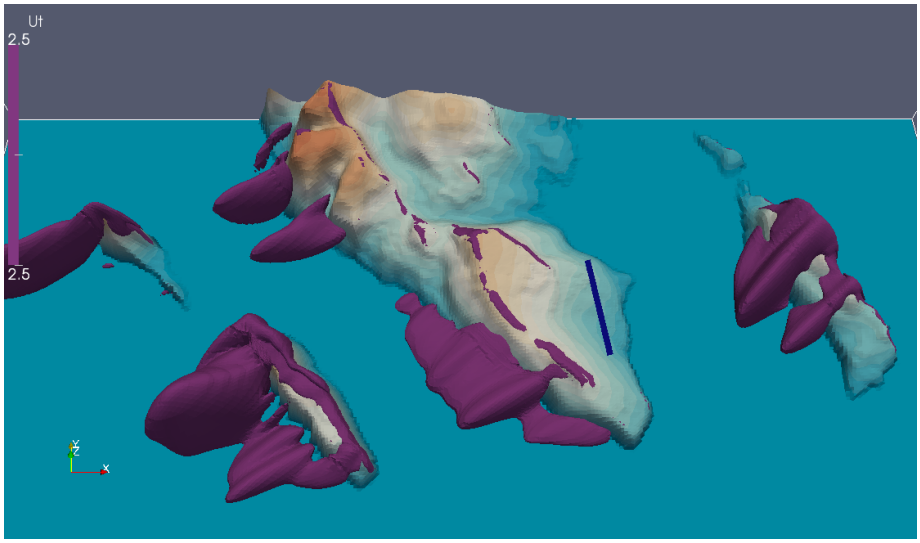

(b)

Figure 12: Iso-surfaces of turbulent velocity U_t at Glyvursnes for northeasterly wind ($\alpha = 225^o$). In (a) and (b) are shown iso-surfaces for $U_t = 2.0$ and $U_t = 2.5$, respectively.

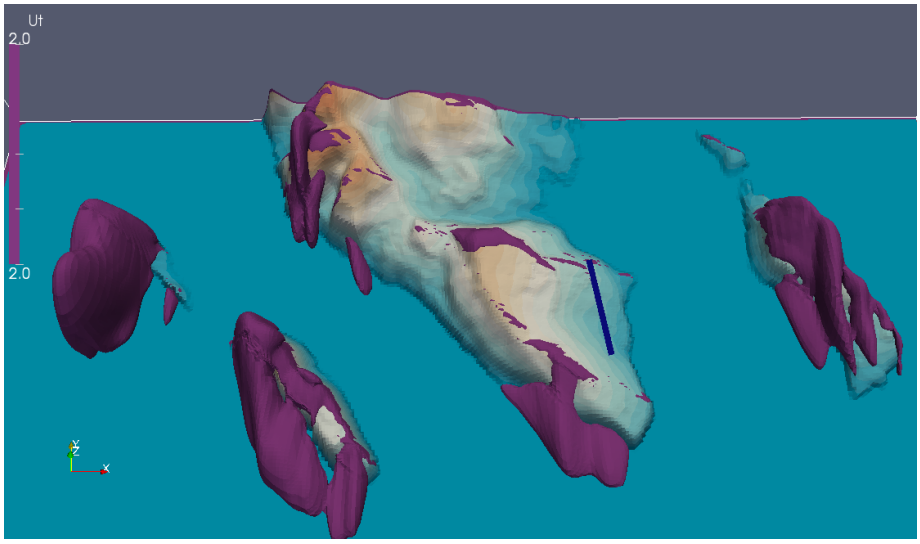

(a)

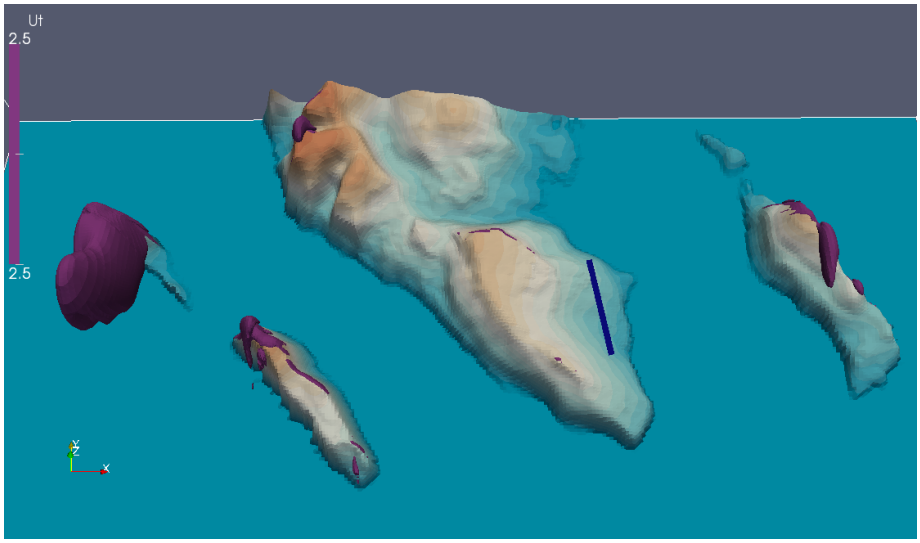

(b)

Figure 13: Iso-surfaces of turbulent velocity U_t at Glyvursnes for northerly wind ($\alpha = 270^o$). In (a) and (b) are shown iso-surfaces for $U_t = 2.0$ and $U_t = 2.5$, respectively.

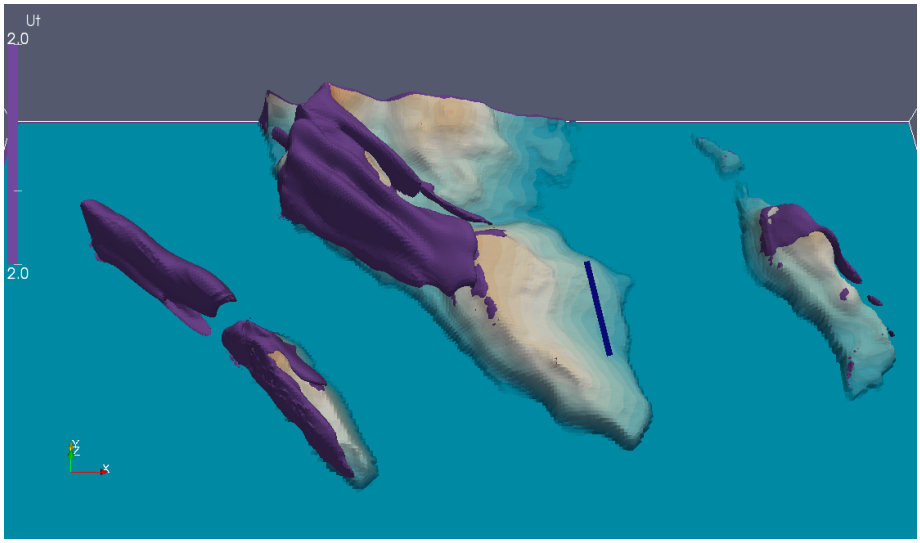

(a)

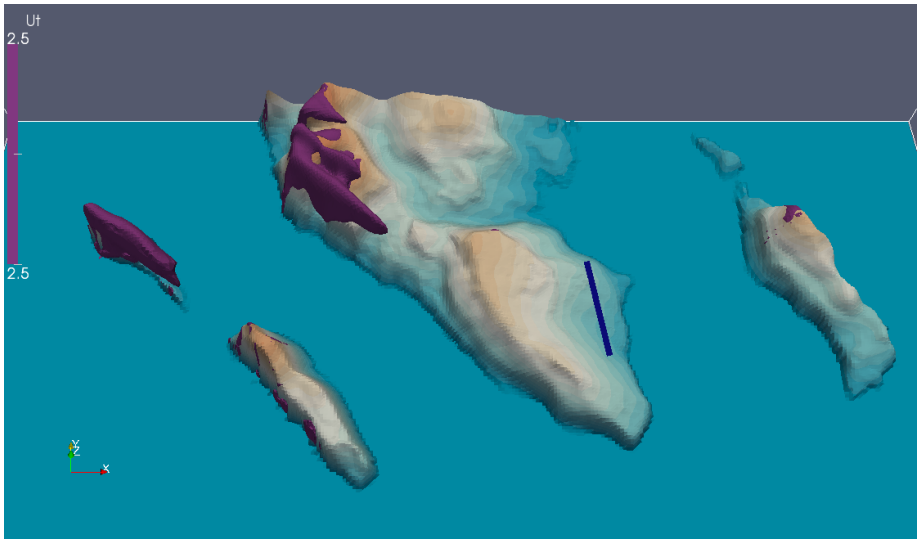

(b)

Figure 14: Iso-surfaces of turbulent velocity U_t at Glyvursnes for northwesterly wind ($\alpha = 315^o$). In (a) and (b) are shown iso-surfaces for $U_t = 2.0$ and $U_t = 2.5$, respectively.

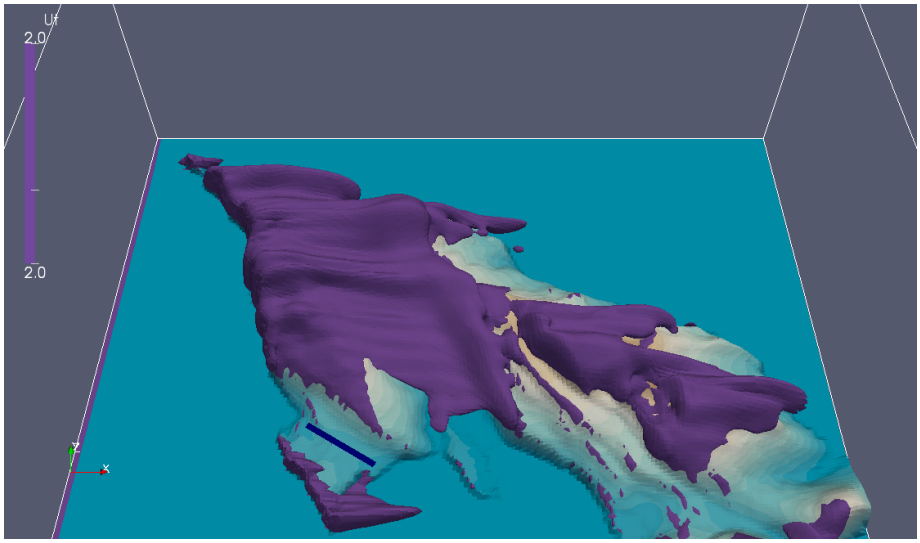

(a)

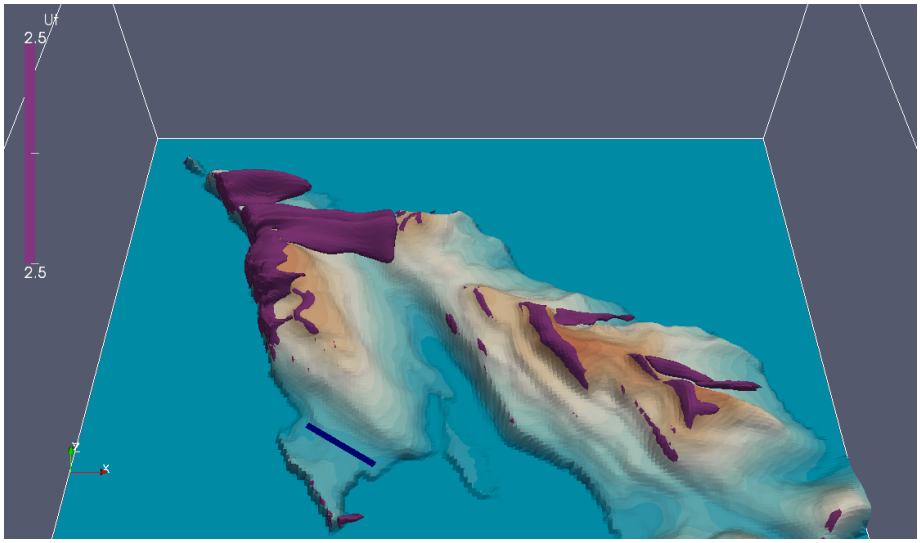

(b)

Figure 15: Iso-surfaces of turbulent velocity U_t at Søltuvik for westerly wind ($\alpha = 0^o$). In (a) and (b) are shown iso-surfaces for $U_t = 2.0$ and $U_t = 2.5$, respectively.

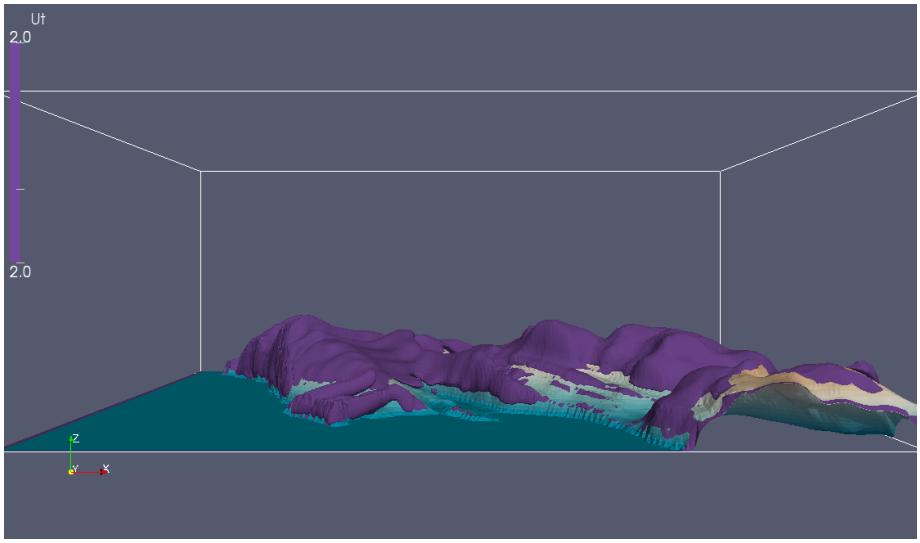

(a)

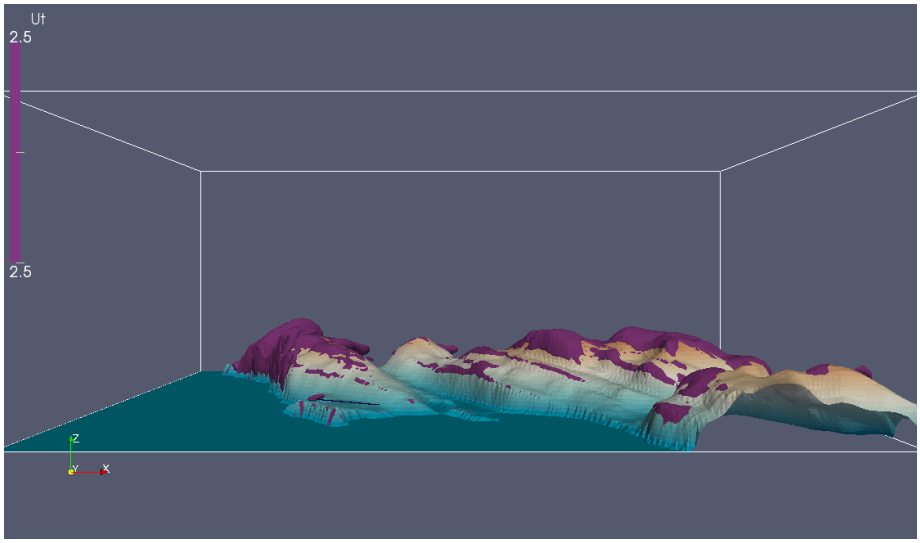

(b)

Figure 16: Iso-surfaces of turbulent velocity U_t at Søltuvik for southwesterly wind ($\alpha = 45^o$). In (a) and (b) are shown iso-surfaces for $U_t = 2.0$ and $U_t = 2.5$, respectively.

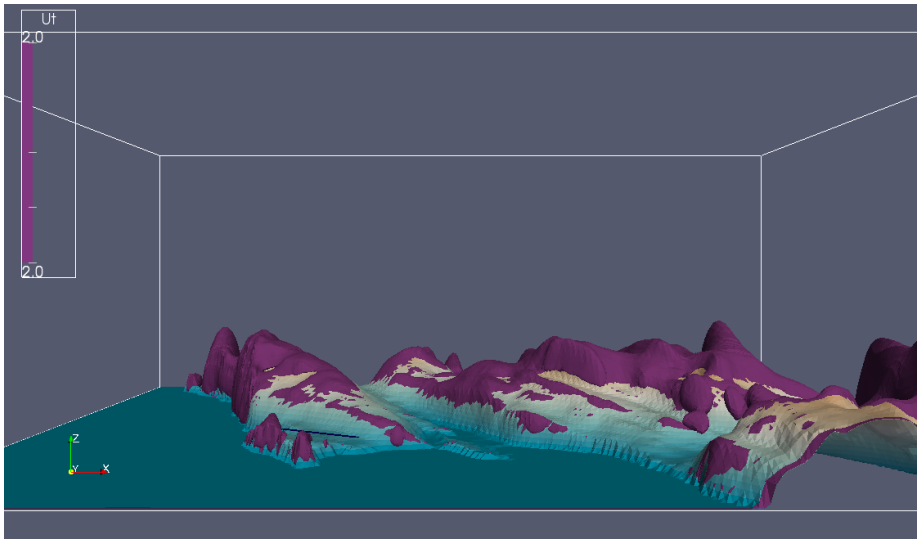

(a)

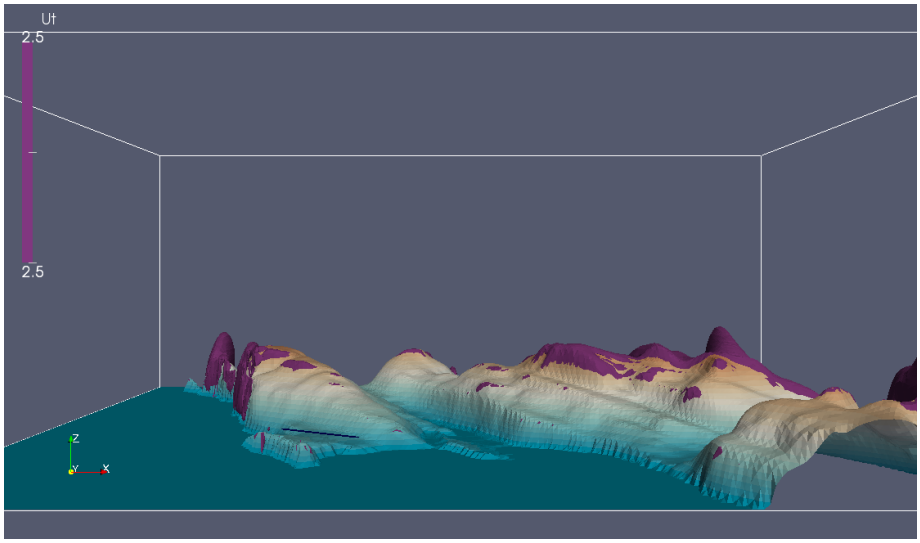

(b)

Figure 17: Iso-surfaces of turbulent velocity U_t at Søltuvik for southerly wind ($\alpha = 90^o$). In (a) and (b) are shown iso-surfaces for $U_t = 2.0$ and $U_t = 2.5$, respectively.

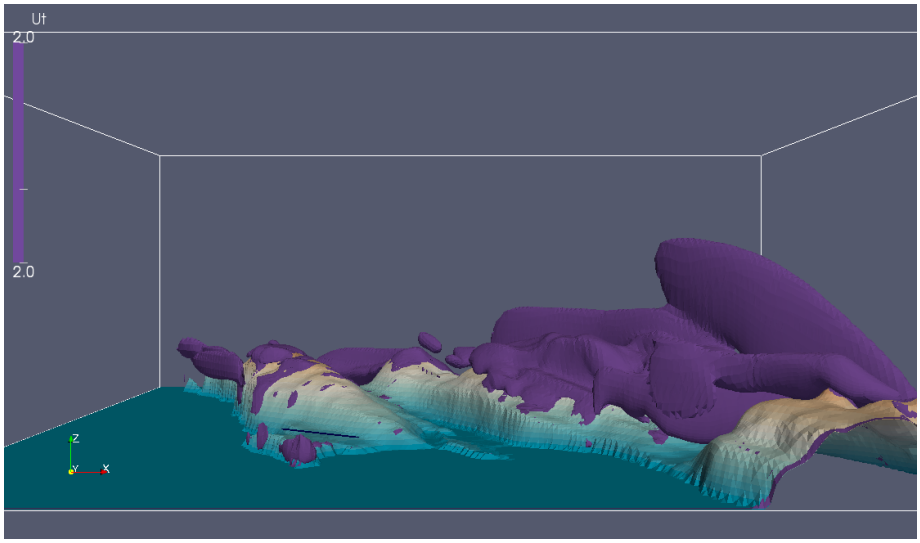

(a)

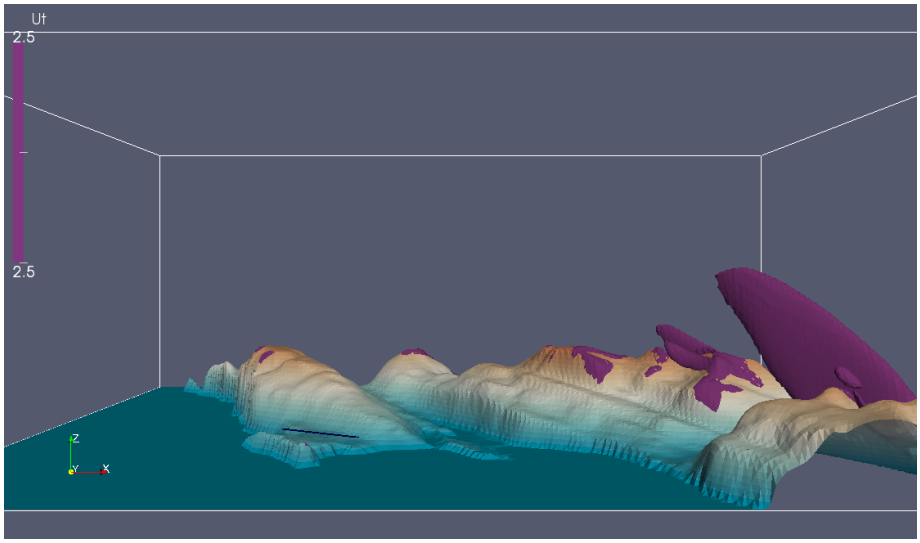

(b)

Figure 18: Iso-surfaces of turbulent velocity U_t at Søltuvik for southeasterly wind ($\alpha = 135^o$). In (a) and (b) are shown iso-surfaces for $U_t = 2.0$ and $U_t = 2.5$, respectively.

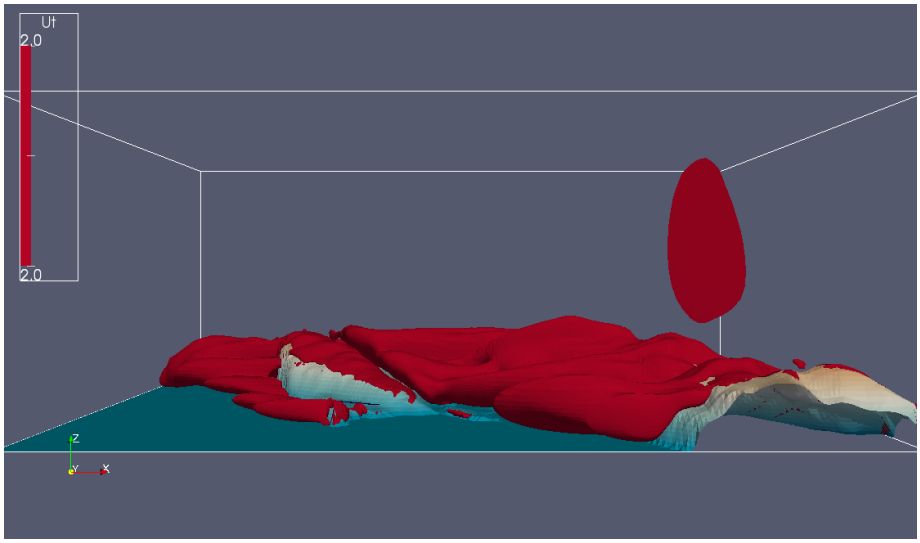

(a)

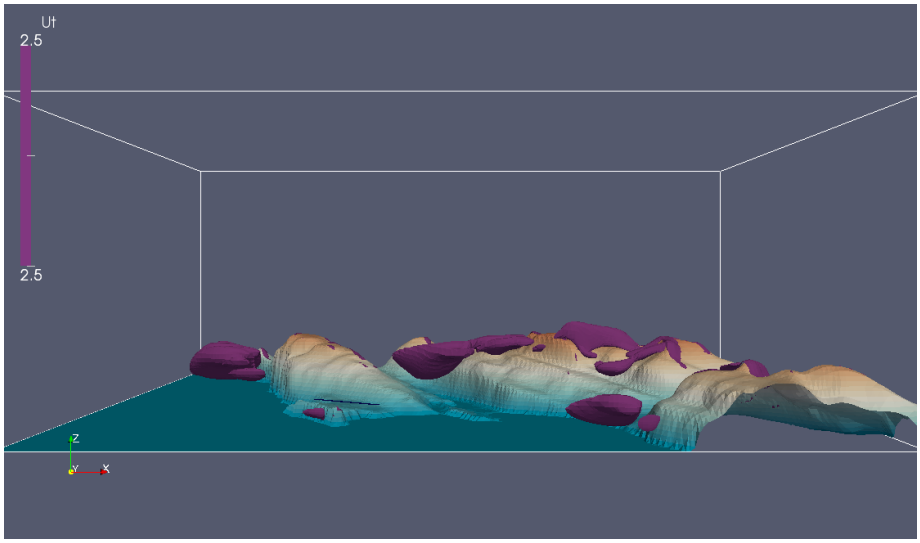

(b)

Figure 19: Iso-surfaces of turbulent velocity U_t at Søltuvik for easterly wind ($\alpha = 180^o$). In (a) and (b) are shown iso-surfaces for $U_t = 2.0$ and $U_t = 2.5$, respectively.

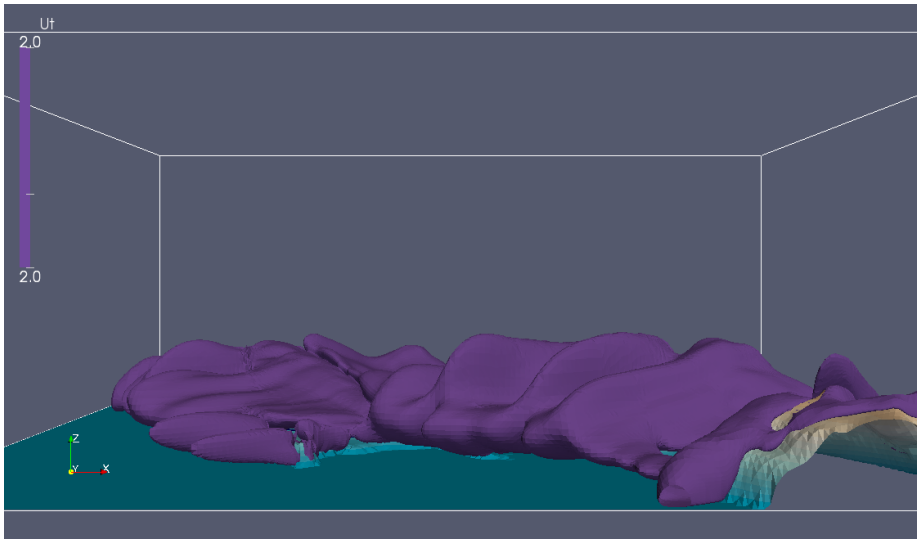

(a)

(b)

Figure 20: Iso-surfaces of turbulent velocity U_t at Søltuvik for northeasterly wind ($\alpha = 225^o$). In (a) and (b) are shown iso-surfaces for $U_t = 2.0$ and $U_t = 2.5$, respectively.

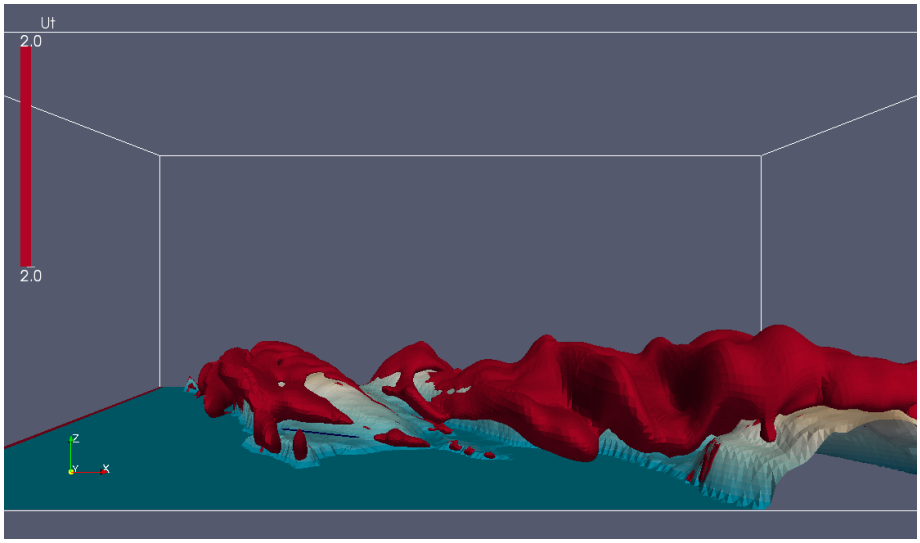

(a)

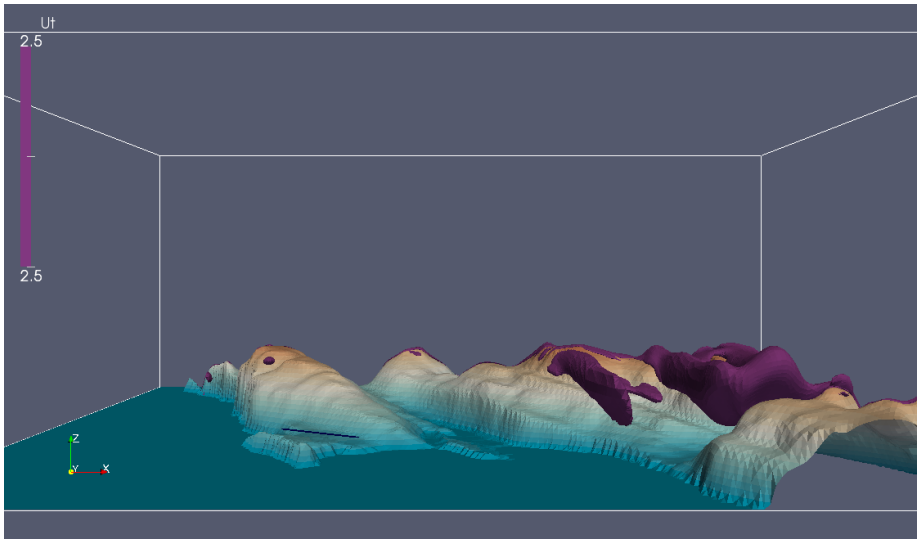

(b)

Figure 21: Iso-surfaces of turbulent velocity U_t at Søltuvik for northerly wind ($\alpha = 270^o$). In (a) and (b) are shown iso-surfaces for $U_t = 2.0$ and $U_t = 2.5$, respectively.

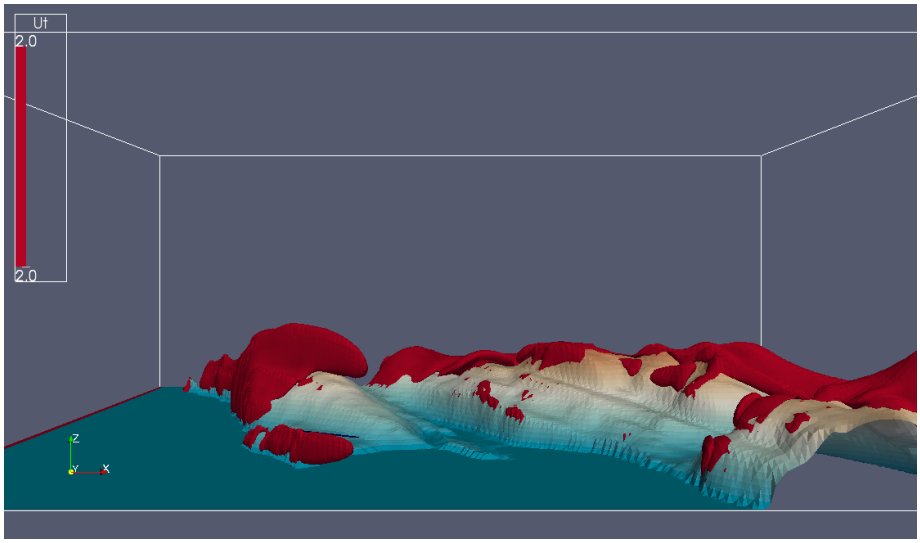

(a)

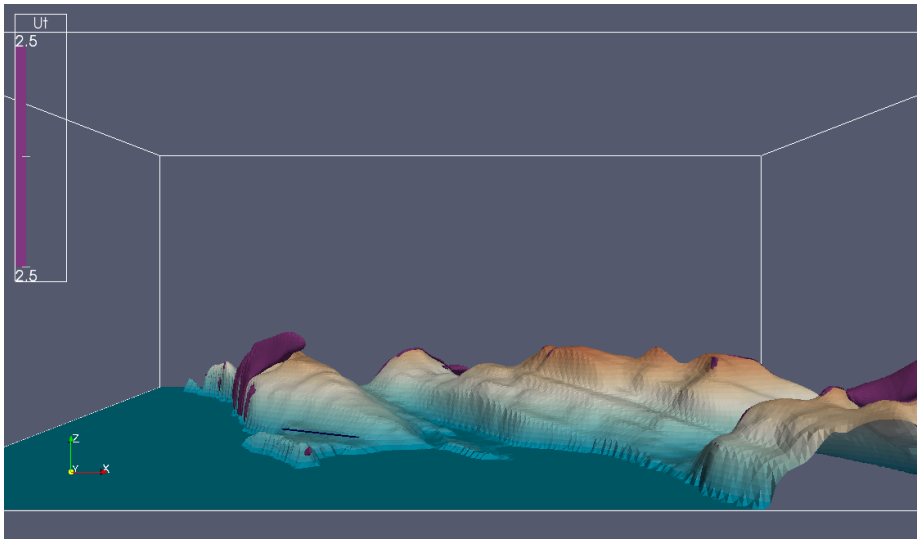

(b)

Figure 22: Iso-surfaces of turbulent velocity U_t at Søltuvik for northwesterly wind ($\alpha = 315^o$). In (a) and (b) are shown iso-surfaces for $U_t = 2.0$ and $U_t = 2.5$, respectively.

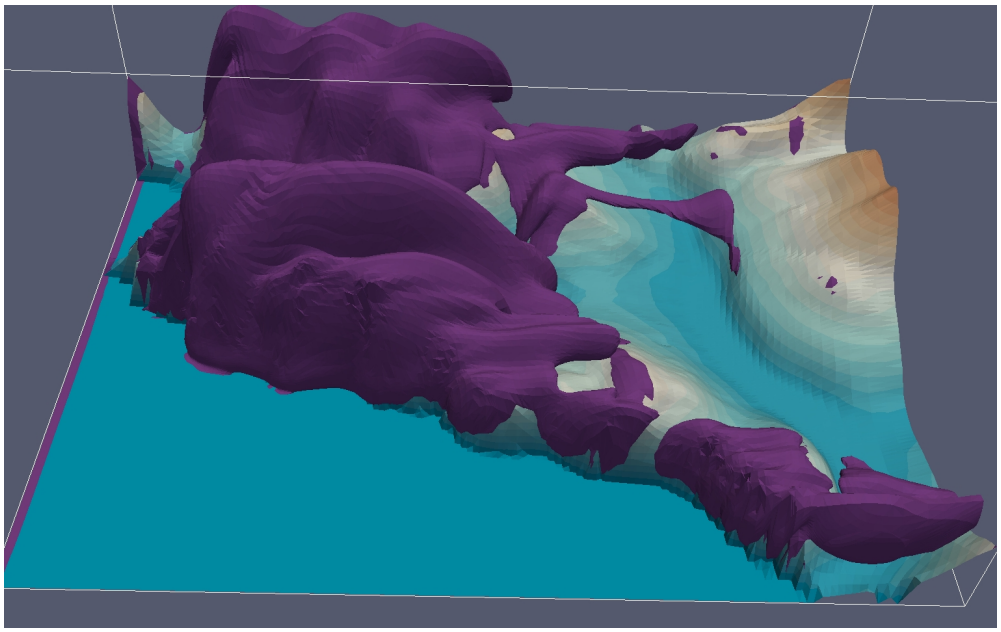

(a)

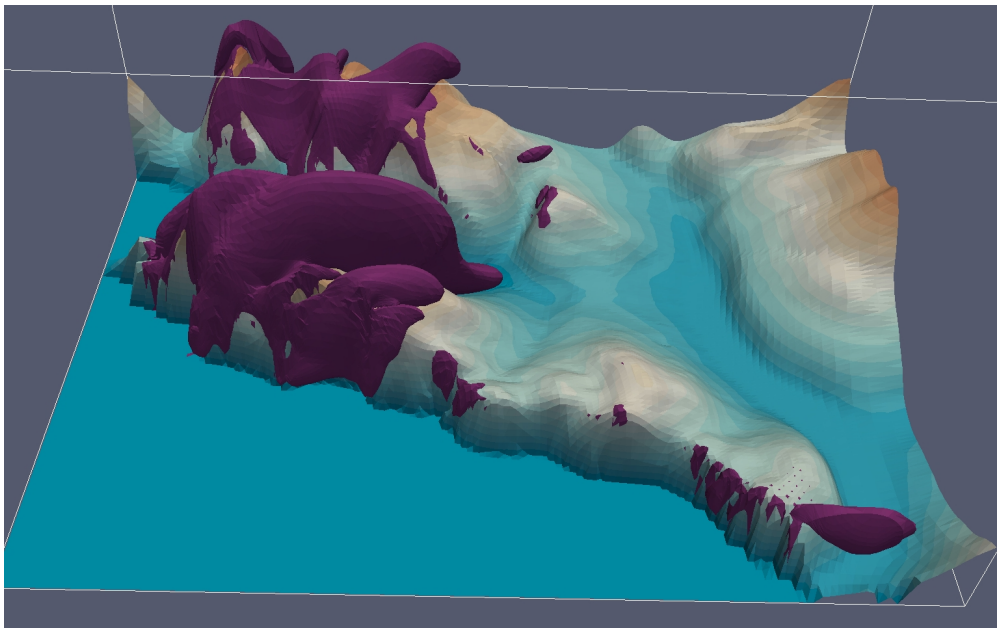

(b)

Figure 23: Iso-surfaces of turbulent velocity U_t at Vágar for westerly wind ($\alpha = 0^o$). In (a) and (b) are shown iso-surfaces for $U_t = 2.0$ and $U_t = 2.5$, respectively.

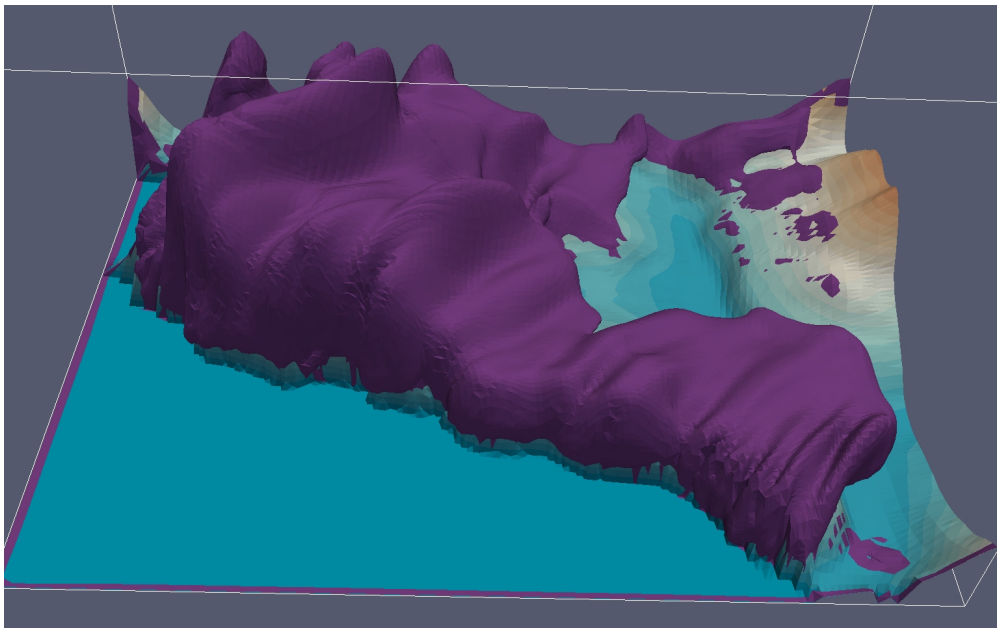

(a)

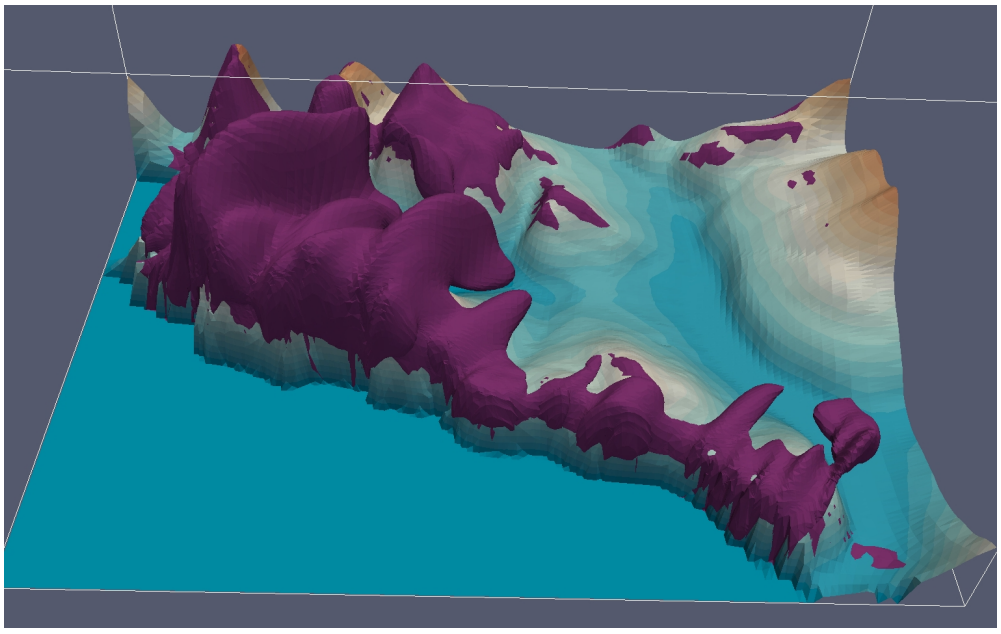

(b)

Figure 24: Iso-surfaces of turbulent velocity U_t at Vágar for southwesterly wind ($\alpha = 45^o$). In (a) and (b) are shown iso-surfaces for $U_t = 2.0$ and $U_t = 2.5$, respectively.

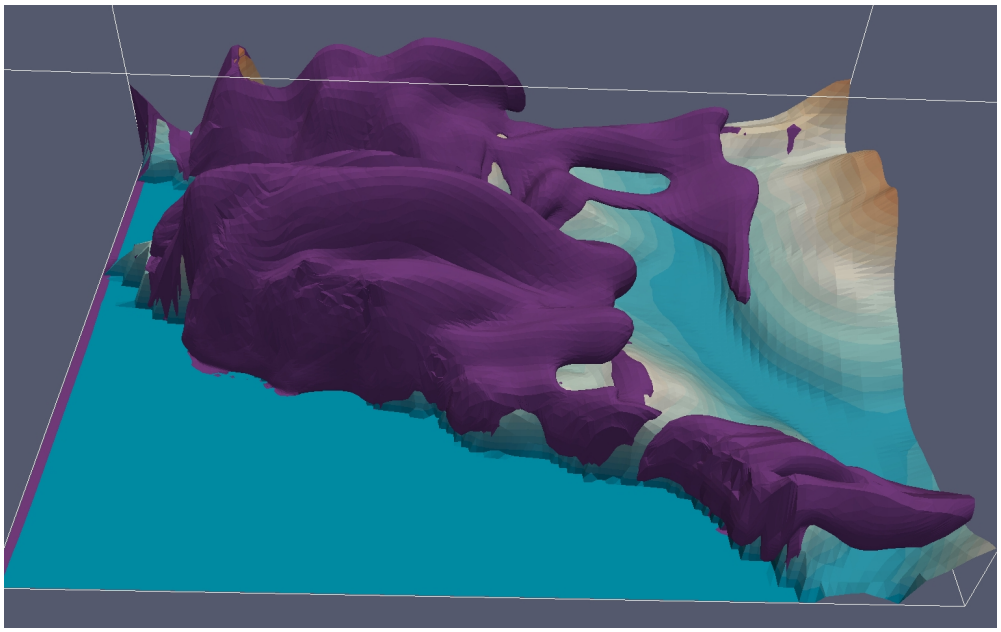

(a)

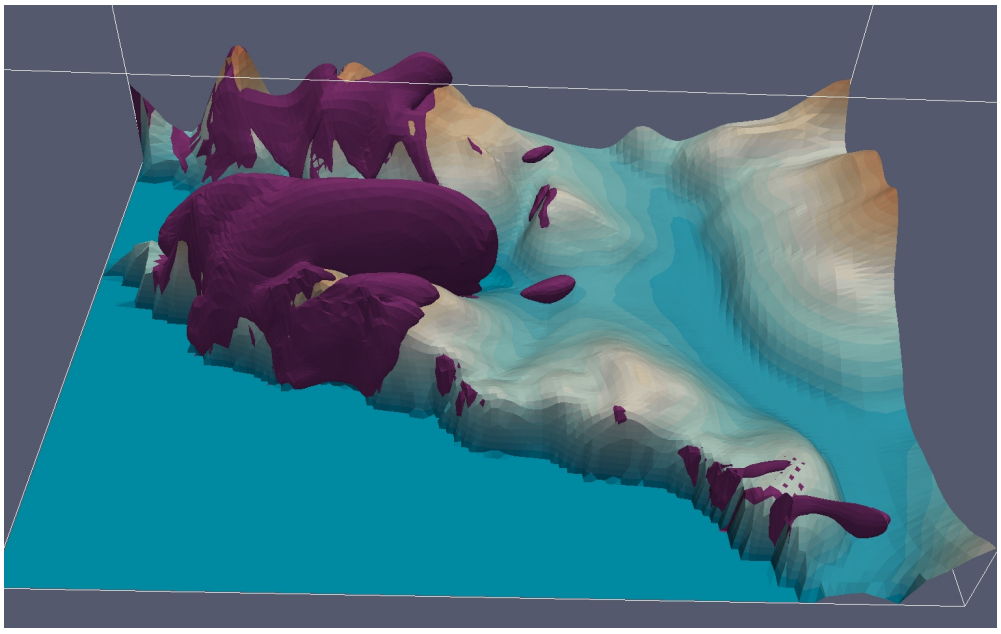

(b)

Figure 25: Iso-surfaces of turbulent velocity U_t at Vágar for southerly wind ($\alpha = 90^o$). In (a) and (b) are shown iso-surfaces for $U_t = 2.0$ and $U_t = 2.5$, respectively.

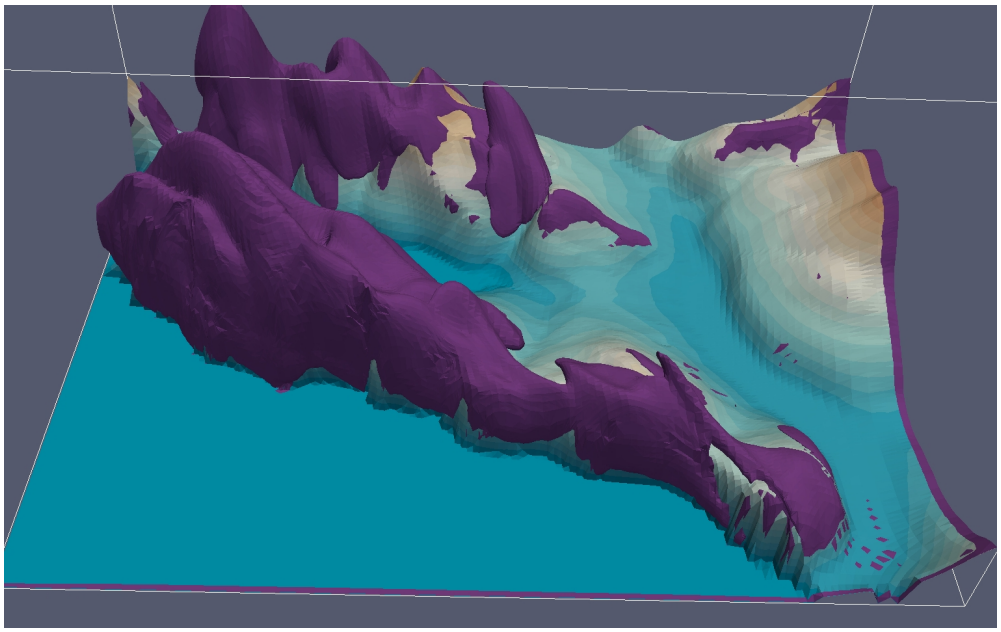

(a)

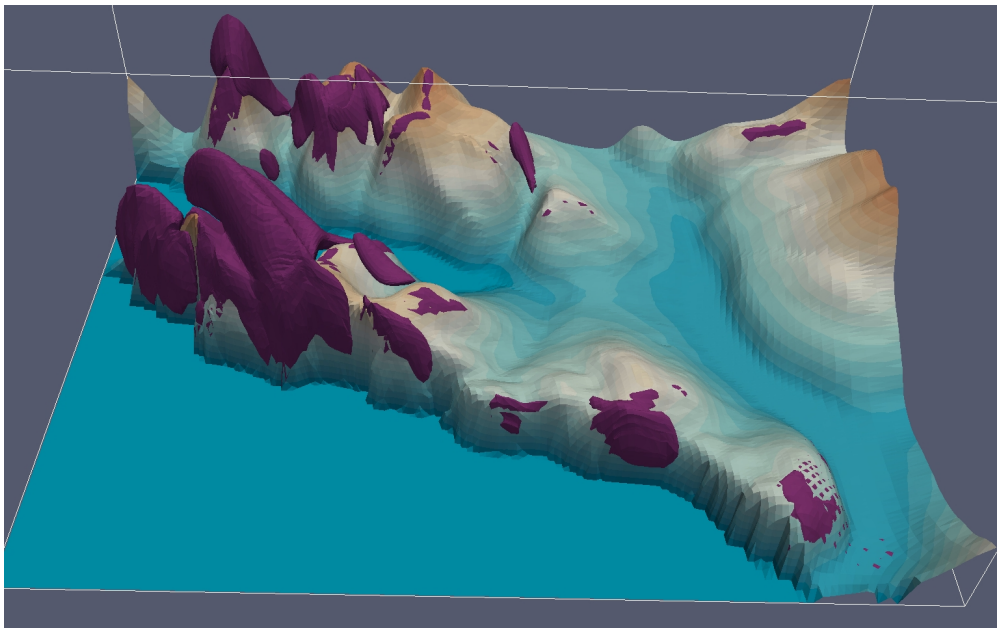

(b)

Figure 26: Iso-surfaces of turbulent velocity U_t at Vágar for southeasterly wind ($\alpha = 135^o$). In (a) and (b) are shown iso-surfaces for $U_t = 2.0$ and $U_t = 2.5$, respectively.

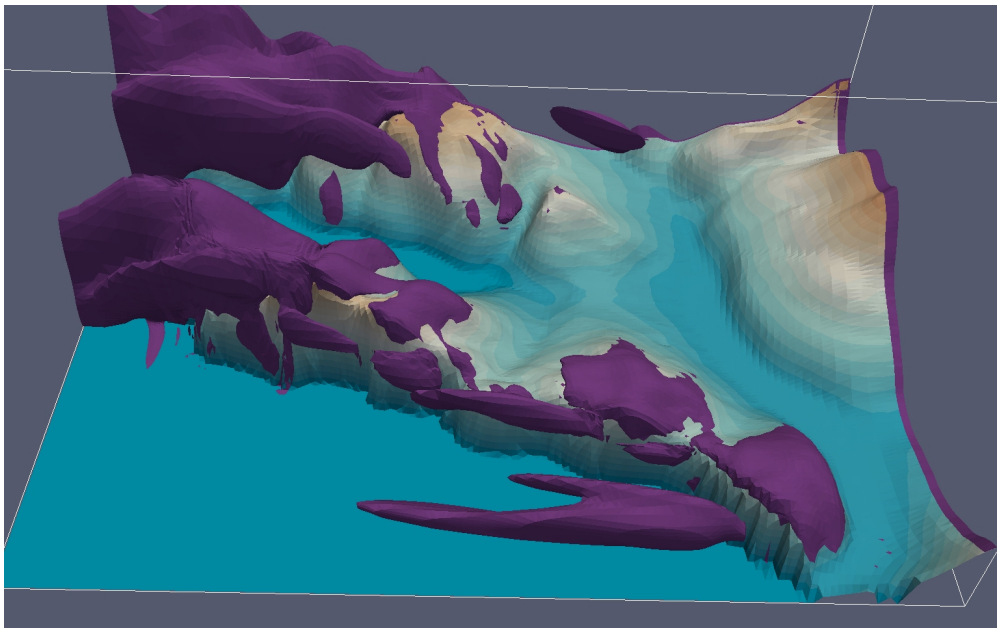

(a)

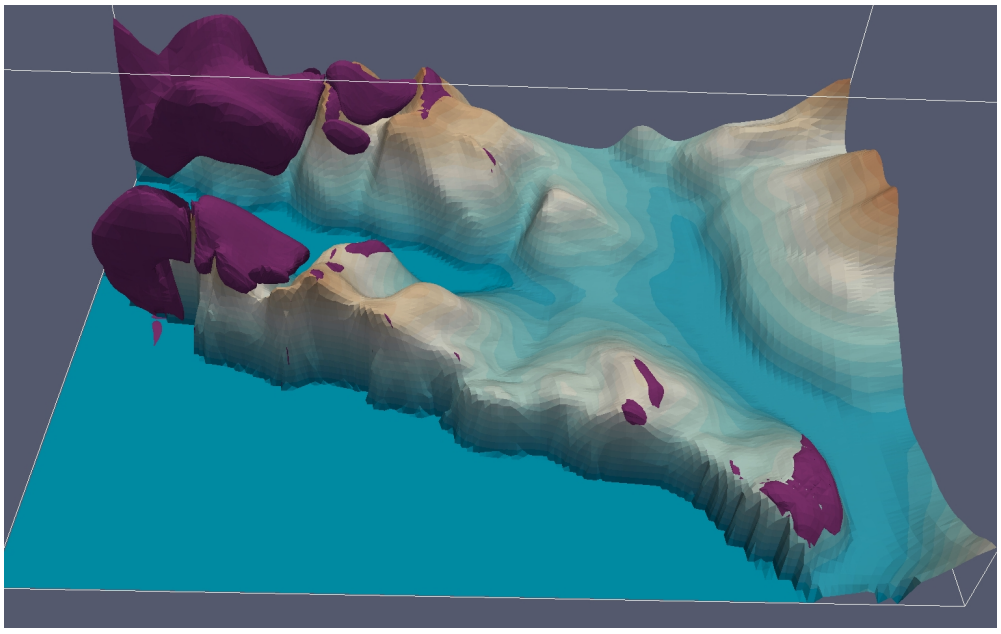

(b)

Figure 27: Iso-surfaces of turbulent velocity U_t at Vágar for easterly wind ($\alpha = 180^o$). In (a) and (b) are shown iso-surfaces for $U_t = 2.0$ and $U_t = 2.5$, respectively.

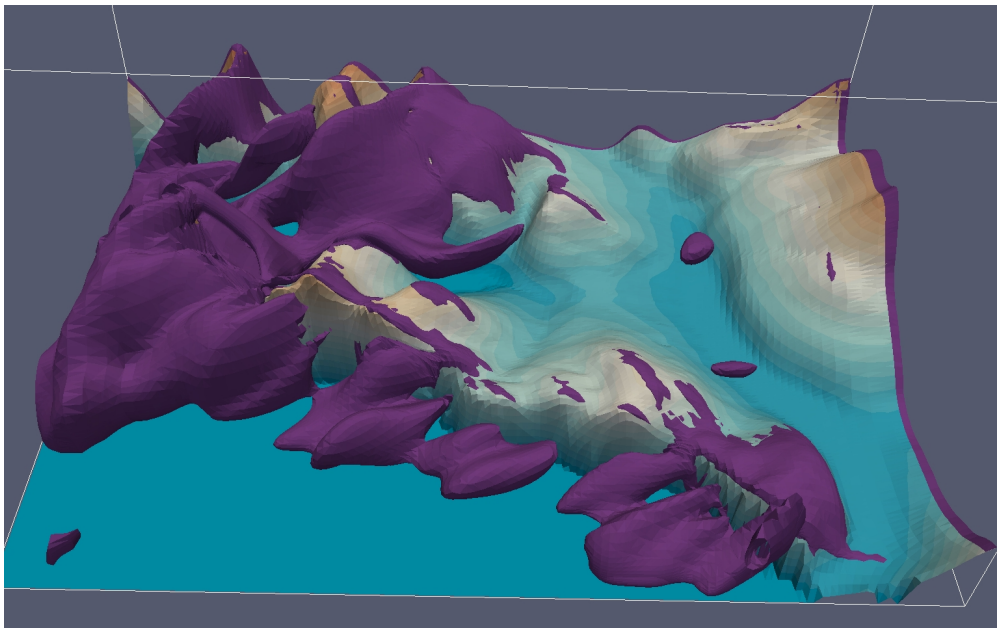

(a)

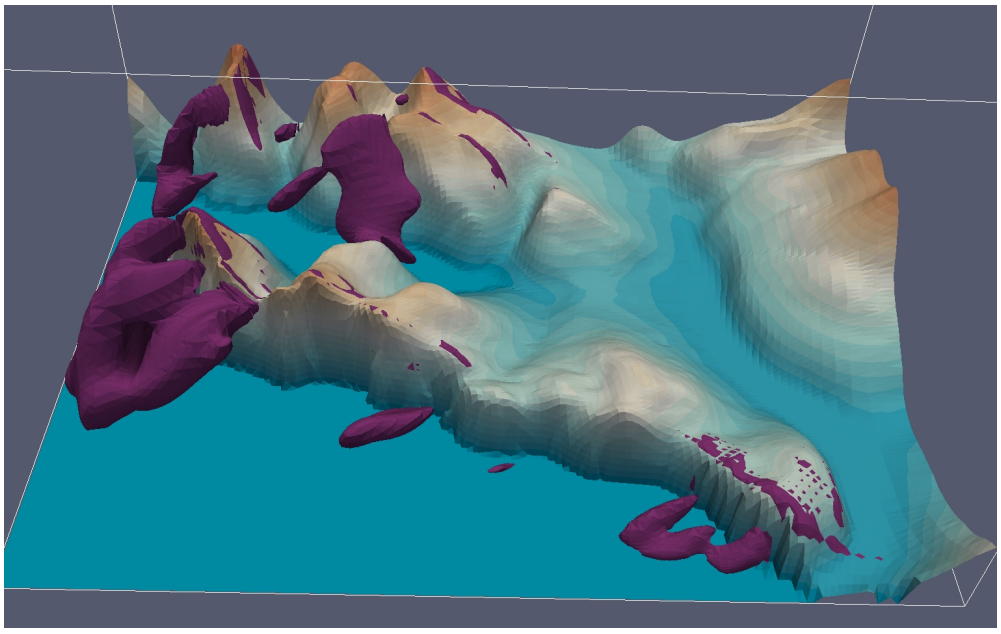

(b)

Figure 28: Iso-surfaces of turbulent velocity U_t at Vágar for northeasterly wind ($\alpha = 225^o$). In (a) and (b) are shown iso-surfaces for $U_t = 2.0$ and $U_t = 2.5$, respectively.

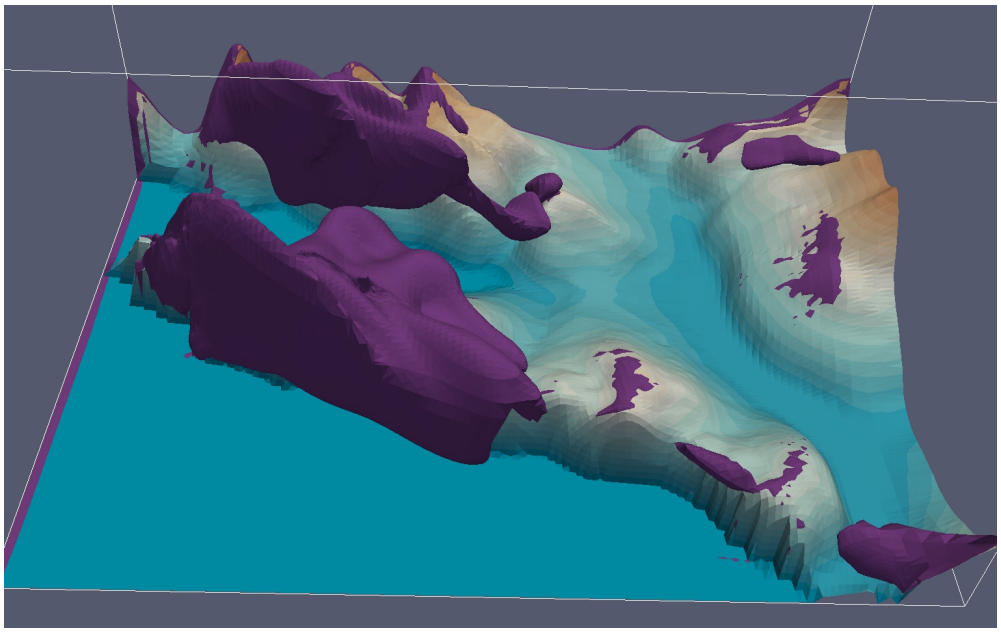

(a)

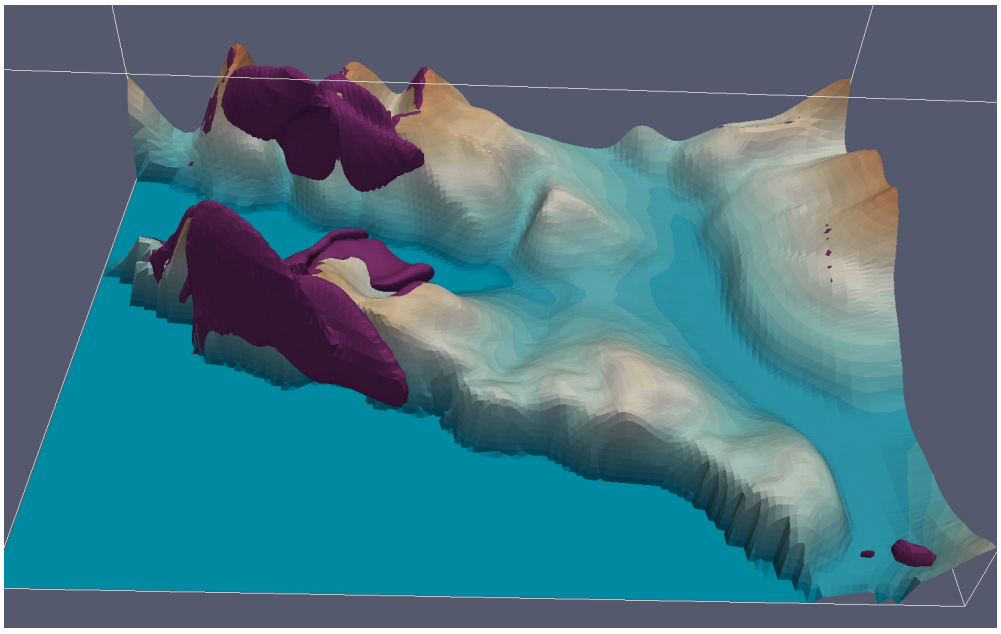

(b)

Figure 29: Iso-surfaces of turbulent velocity U_t at Vágar for northwesterly wind ($\alpha = 315^o$). In (a) and (b) are shown iso-surfaces for $U_t = 2.0$ and $U_t = 2.5$, respectively.

5 Conclusion

In this work we conducted a detailed analysis for three alternate locations: Glyvursnes, Søltuvik and Vágar as a potential site for a future airport. The study analyzed only the terrain induced turbulence at these sites. Based on the observations presented in the last section we can enumerate the most important findings:

1. The Glyvursnes location is the best of the three alternate locations. The reasons according to the study are the aerodynamic shape of the coastal region to the south, north and east of the runway and its location far away from the cliffs on the western side. Søltuvik has unfavorable flight conditions due to the cliff on the western side which has a strong local effect and the high hill on the north eastern side which causes much larger scale phenomenon. The third location Vágar is also surrounded by hills on the north and south side. From the simulation it appears that the northerly, northeasterly, southerly and southwesterly are problematic wind directions. It will be interesting to know the experience of the pilots who operate in the region.

2. From the windrose diagram given in [6] we see that the wind speed at $10\,m$ above the ground occasionally reaches $13m/s$ implying a free stream speed of $30m/s$ (assuming the idealized logarithmic profile). In such a situation the contours of $u_t = 2.5$ (presented in the figures) which are otherwise well below the critical value of 3.5 could actually become dangerous for aviation activities.

3. Steep cliffs and high hills lead to flow separation resulting in an intense turbulence on the leeward side. This is a common trend observed in all the simulations presented in this report. Due to the unavailability of the potential temperature profile (stratification) mountain waves could not be simulated in his study. Past experience says that these can further worsen flight conditions. Their effects will be more pronounced at Søltuvik and Vágar as they have ideal configuration of hills for the generation of these waves. Glyvursnes will be least affected by the phenomenon.

It should be worth stressing here that in the present study we have just concentrated on the terrain induced turbulence which is a local phenomenon. Studying the effects of large scale meteorological phenomena on the site is beyond the capabilities of the model we used. A nested approach with different models capable of resolving different scales coupled together can be more effective in analyzing such sites. For example gusts and down-drafts due to shower activities are not possible to model with the simulation tool used in our present study. Nevertheless, the simulations have been successful in getting a better insight into the terrain induced turbulence which we think will be a big factor in affecting the aviation activities in the regions under investigation.

Acknowledgement

We are thankful to Klæmint Østerø for providing terrain data of the concerned site which formed the basis of the present study. We are also thankful to him for going through the report and giving his feedbacks which immensely helped in giving the report its present form. Thanks are also due to Helge Midtbø for his comments and feedback during the course of simulations. We would also like to thank Marit Ødegard for giving this report the final touch.

References

[1] PR Bannon. Potential vorticity conservation, hydrostatic adjustment and the anelastic approximation. *Journal of Atmospheric Science*, 52:2302–2312, 1995.

[2] TL Clark, T Keller, J Coen, P Neilley, H-M Hsu, and ED Hall. Terrain-induced Turbulence over Lantau Island: 7 june 1994 tropical storm russ case study. *Journal of Atmospheric Science*, 54:1795–1814, 1997.

[3] DR Durran. Numerical methods for wave equations in geophysical fluid dynamics. *Springer*, 1998.

[4] KJ Eidsvik, A Holstad, and T Utnes. A prediction system for local wind variation in mountainous terrain. *Boundary Layer Meteorology*, 112:557–586, 2004.

[5] V Haroutunian, W Minkowycz, and Shyy. General algorithms for the finite element solution of incompressible flow problems using primitive variables. *Advances in Numerical Heat Transfer*, 1:5305–5328, 1997.

[6] K Harstveit. Færøyene - analyse av meteorlogiske forhold på mulig ny flyplass. *Kjeller Vindteknikk*, (KVT/KH/2010/R017), 2010.

[7] W Rodi. Examples of calculation methods for flow and mixing in stratified fluids. *Journal of Geophysics*, 92 C5:5305–5328, 1987.

[8] T Utnes. Modelling of stratified geophysical flows over variable topography. *Geometric Modelling, Numerical Simulation and Optimization*, ISBN 978-3-540-68782-5:361–390, 2007.

[9] T Utnes. A segregated implicit pressure projetion method for turbulent flows. *SINTEF Applied Mathematics*, Report A1686, 2007.

Technology for a better society

www.sintef.no